



HAL
open science

Fluid-Driven Shear Instabilities in the Subducted Oceanic Mantle at Intermediate Depths: Insights From Western Alps Meta-Ophiolites

Jesus Muñoz-Montecinos, Samuel Angiboust, Clothilde Minnaert, Alberto Ceccato, Luiz Morales, Julien Gasc, Whitney Behr

► **To cite this version:**

Jesus Muñoz-Montecinos, Samuel Angiboust, Clothilde Minnaert, Alberto Ceccato, Luiz Morales, et al.. Fluid-Driven Shear Instabilities in the Subducted Oceanic Mantle at Intermediate Depths: Insights From Western Alps Meta-Ophiolites. *Geochemistry, Geophysics, Geosystems*, 2024, 25 (8), pp.e2024GC011581. 10.1029/2024gc011581 . hal-04814946

HAL Id: hal-04814946

<https://hal.science/hal-04814946v1>

Submitted on 2 Dec 2024

HAL is a multi-disciplinary open access archive for the deposit and dissemination of scientific research documents, whether they are published or not. The documents may come from teaching and research institutions in France or abroad, or from public or private research centers.

L'archive ouverte pluridisciplinaire **HAL**, est destinée au dépôt et à la diffusion de documents scientifiques de niveau recherche, publiés ou non, émanant des établissements d'enseignement et de recherche français ou étrangers, des laboratoires publics ou privés.



Distributed under a Creative Commons Attribution 4.0 International License

Geochemistry, Geophysics, Geosystems®



RESEARCH ARTICLE

10.1029/2024GC011581

Key Points:

- Transient brittle-ductile deformation of serpentinites within the Intermediate Depths Seismicity window
- Dilational and hybrid mode dilational-shear olivine-bearing veins suggest high, potentially near-lithostatic, fluid pressure conditions
- Shear strain concentrates along the margins of ultramafic slivers, enhancing permeability and fluid flow at (ultra)high pressure conditions

Supporting Information:

Supporting Information may be found in the online version of this article.

Correspondence to:

J. Muñoz-Montecinos,
jmunoz@ethz.ch

Citation:

Muñoz-Montecinos, J., Angiboust, S., Minnaert, C., Ceccato, A., Morales, L., Gasc, J., & Behr, W. (2024). Fluid-driven shear instabilities in the subducted oceanic mantle at intermediate depths: Insights from Western Alps meta-ophiolites. *Geochemistry, Geophysics, Geosystems*, 25, e2024GC011581. <https://doi.org/10.1029/2024GC011581>

Received 26 MAR 2024

Accepted 23 JUL 2024

© 2024 The Author(s). Geochemistry, Geophysics, Geosystems published by Wiley Periodicals LLC on behalf of American Geophysical Union. This is an open access article under the terms of the [Creative Commons Attribution-NonCommercial-NoDerivs License](https://creativecommons.org/licenses/by/4.0/), which permits use and distribution in any medium, provided the original work is properly cited, the use is non-commercial and no modifications or adaptations are made.

Fluid-Driven Shear Instabilities in the Subducted Oceanic Mantle at Intermediate Depths: Insights From Western Alps Meta-Ophiolites

J. Muñoz-Montecinos¹ , S. Angiboust^{2,3,4}, C. Minnaert^{2,4}, A. Ceccato¹ , L. Morales^{1,5} , J. Gasc⁶, and W. Behr¹ 

¹Department of Earth and Planetary Sciences, Structural Geology and Tectonics Group, Geological Institute, ETH Zürich, Zürich, Switzerland, ²Laboratoire de Géologie de Lyon (LGL-TPE), Ecole Normale Supérieure de Lyon, Lyon, France, ³Institut Universitaire de France (IUF), Paris, France, ⁴Institut de Physique du Globe de Paris, Université Paris Cité, Paris, France, ⁵Scientific Centre for Optical and Electron Microscopy (ScopeM), ETH Zürich, Zürich, Switzerland, ⁶Laboratoire de Géologie, Ecole Normale Supérieure, Paris, France

Abstract Serpentinites are major carriers of volatiles in deep subduction zones, releasing most fluids in the 500–650°C range. Despite fundamental implications for mass transfer and intermediate-depth seismicity, the mechanical role of these fluids is unclear. To characterize the mechanical role of fluids at (ultra)high-pressure conditions, we perform a petro-structural analysis on olivine-rich veins from the Western Alps meta-ophiolite. Some veins formed through dilational and mixed dilational-shear fracturing without significant shear-related deformation. However, field and microstructural observations indicate transient shearing and dilational fracturing at high pore fluid pressures. These include: (a) foliated sheared veins; (b) newly formed olivine and Ti-clinohumite within mineral lineations coating sheared veins and shear bands; (c) Olivine and Ti-clinohumite mineral fibers sealing porphyroclasts; (d) mutual crosscutting relationships among dilational and shear features. Dilational veins prevail in low-strain areas, while sheared veins and shear bands dominate within high-strain zones toward the ultramafic sliver boundaries. These strain variations underscore the role of local stress regimes during serpentinite dehydration. Consequently, areas experiencing stronger shear stresses around large-scale blocks or mechanical weakening during fluid circulation are prone to draining overpressurized fluids. These interface-parallel and fracture-controlled pathways thus facilitate fluid escape from the dehydrating downgoing slab. Transient events of dilational fracturing and brittle-ductile shearing, along with strain localization in highly comminuted olivine-bearing sheared veins, may have resulted from strain rate bursts potentially related to (sub)seismic deformation. These observations are in line with geophysical data indicating high pore fluid pressures within the intermediate-depth seismicity region.

1. Introduction

Serpentinites are major carriers of volatiles in subduction zones (Bach & Früh-Green, 2010; Klein et al., 2020). The oceanic mantle contains up to 13 wt% of H₂O in fully serpentinitized cases, typically representing slow-spreading ridge settings. These fluids are released by devolatilization reactions (Figure 1) down to depths of ~200 km (Padrón-Navarta et al., 2013; Ulmer & Trommsdorff, 1995), far beyond those of metamafic lithologies, which release their H₂O at depths of ~70 km during blueschist-to eclogite-forming reactions (Schmidt & Poli, 1998). These fluids play a critical role in geodynamic and tectonic processes (Hacker et al., 2003; Menant et al., 2019; Peacock & Hyndman, 1999), but their interaction with deformation within the subducting slab is challenging to probe and to reproduce experimentally (Ferrand et al., 2017; Reynard, 2013).

The subducting slab is regarded as a fluid overpressurized environment, with fluid pressures exceeding hydrostatic, and transiently surpassing lithostatic levels (Audet & Kim, 2016; Bloch et al., 2018; Moreno et al., 2014). The fluids circulating therein thus trigger brittle failure and mechanical instabilities (Angiboust et al., 2012; Behr et al., 2018; Davies, 1999; Muñoz-Montecinos, Angiboust, Garcia-Casco, Glodny, & Bebout, 2021; Sibson, 2013; Taetz et al., 2018) when the ratio of fluid pressure to lithostatic pressure ($\lambda_f = P_f/\sigma_v$) exceeds 0.9 (near-lithostatic) or even surpasses 1 (fluid overpressure; Sibson, 2013). The generation of earthquakes is a major outcome of this process (Hacker et al., 2003; Moreno et al., 2014; Muñoz-Montecinos, Angiboust, & Garcia-Casco, 2021). Earthquakes occurring at depths of 50–300 km are

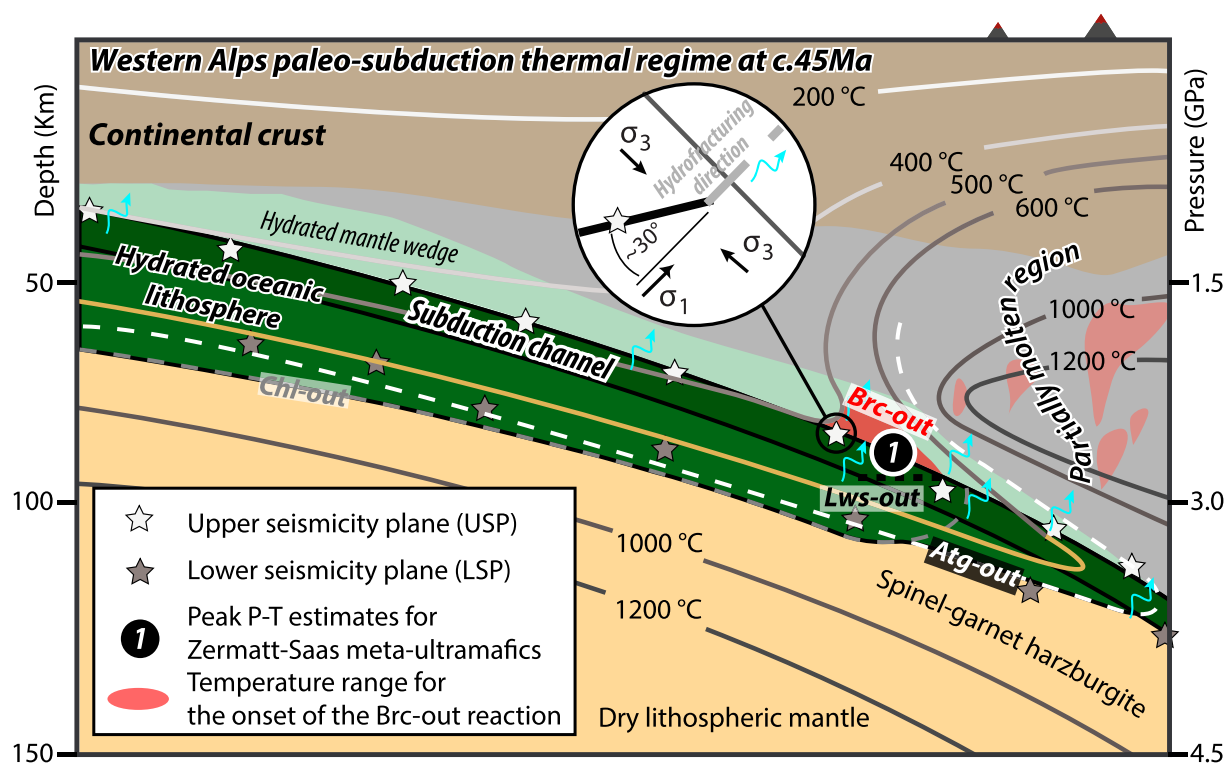


Figure 1. Illustration of a subduction zone depicting major dehydration reactions (according to Schmidt and Poli (2013) and Kempf et al. (2020)). The location of the Upper and Lower seismicity planes is after Hacker et al. (2003) and has been compiled from other active margins which may not necessarily be representative of IDEQs in the Alpine setting. The inset showing potential fluid transport toward the mantle is after Davies (1999). The subduction thermal structure is after Dragovic et al. (2020). Mineral abbreviations after Whitney and Evans (2010).

known as Intermediate depth earthquakes (IDEQs) and, unlike shallow seismicity, little is known on their source mechanisms. IDEQs are characterized by double seismicity planes—an upper (USP) atop of the subducting slab and a lower (LSP) lying tens of kilometers within the downgoing plate (Cabrera et al., 2021; Hacker et al., 2003; Isacks & Barazangi, 1977; Isacks & Molnar, 1971; Sippl et al., 2022). While the origin of LSP events remains debated (Andersen et al., 2014), dehydration reactions in the uppermost mafic/ultramafic section of the subducting slab may control the generation and distribution of USP (Angiboust et al., 2012; Hacker et al., 2003; Hasegawa & Nakajima, 2017; John & Schenk, 2006; Okazaki & Hirth, 2016; Wagner et al., 2020). Therefore, characterizing the mechanisms of dehydration and fluid circulation pathways in this dynamic and deforming environment is key to understanding the physical mechanisms operating in the IDEQs window.

A number of dehydration reactions are possible within the upper-most section of subducting slabs, with one of the most prominent being the antigorite-out reaction. Recent investigations demonstrate that the antigorite-out dehydration reaction to olivine + orthopyroxene releases ~10 wt% of H₂O in the 600–700°C range (Eberhard et al., 2023; Padrón-Navarta et al., 2013). Furthermore, Gasc et al. (2017) observed antigorite dehydration products at 500–600°C—a temperature range consistent with the Brucite + Antigorite = 2Olivine + 3H₂O reaction. The role of brucite dehydration was classically thought to be minor due to its apparently low abundance in serpentinites, and experimental investigations considering brucite-bearing serpentinites are scarce (e.g., Nagaya et al., 2022). However, Klein et al. (2020) showed that brucite is indeed abundant in oceanic serpentinites, underscoring the need for further studies.

Theoretical and laboratory studies thus suggest serpentinite dehydration as a trigger of mechanical instabilities, and natural outcrops further support this finding (Jabaloy-Sánchez et al., 2022; Kempf et al., 2020). In the Western Alps, investigations on an outcrop in the lower Theodul Glacier locality (Zermatt-Saas unit (ZSU); Figure 2a) emphasized that brucite + antigorite dehydration products are widespread in the form of metamorphic

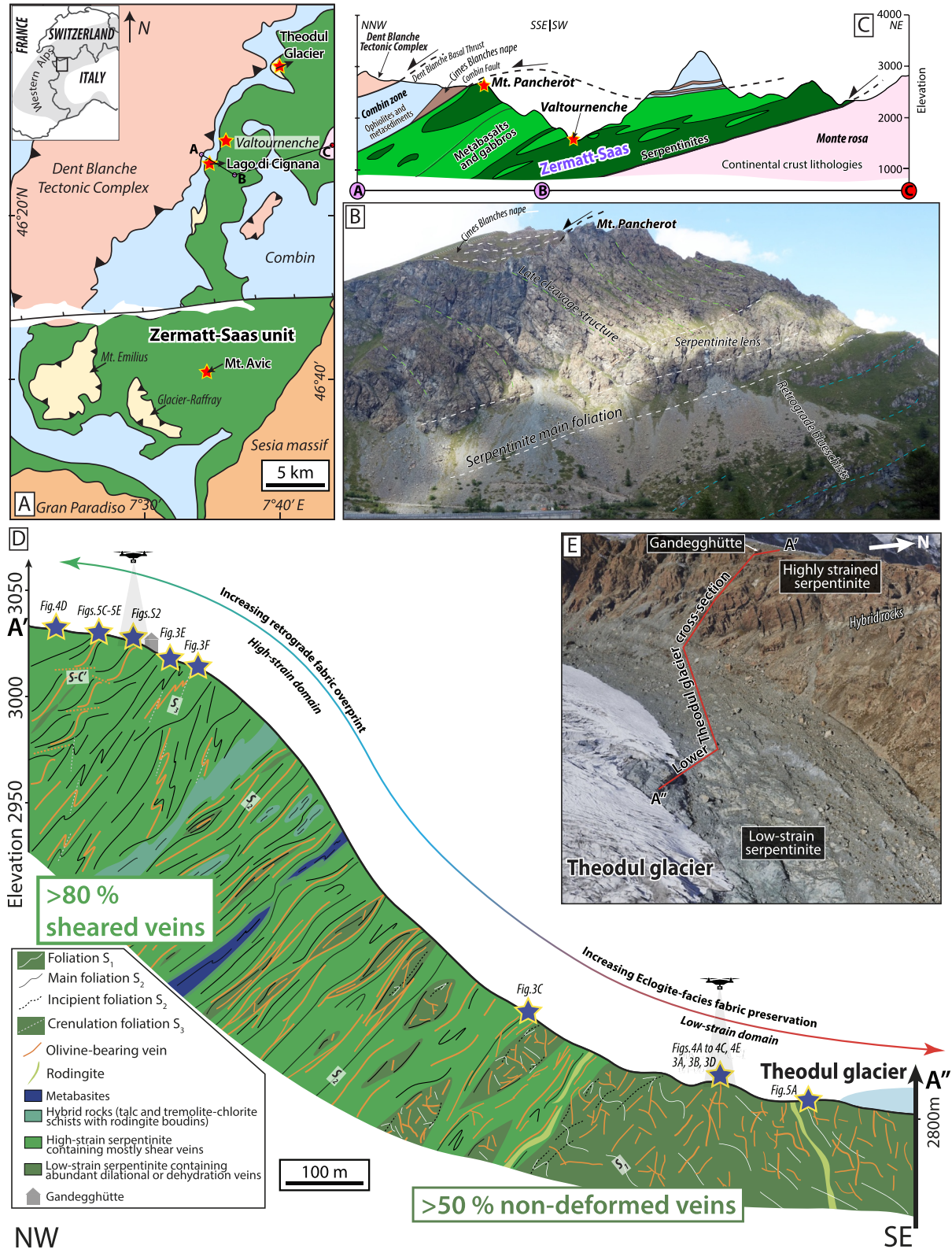


Figure 2.

olivine + Ti-clinohumite + diopside (\pm Ti-chondrodite)-bearing veins (Kempf et al., 2020). These veins originated at (U)HP conditions (Kempf et al., 2020; Peters et al., 2020), but the mechanisms by which the fluids escaped the dehydration front are debated and their role during deformation is unknown. Some authors suggest the (U)HP veins formed in multiple events of cyclic dehydration embrittlement and seismicity (Healy et al., 2009), while others propose a static, non-seismogenic model in which the fluids are drained into permeability pathways resulting from reaction-induced porosity (Plümper et al., 2017).

In this study, we present a multi-scale, petro-structural investigation of metamorphic vein networks in key localities from the Western Alps meta-ophiolites (Figure 2a) to characterize the mechanical role of fluids under (U)HP conditions. The meta-ophiolites exposed in the Western Alps formed in a slow-spreading ridge setting, where serpentinization is likely more intense than in fast spreading settings (Früh-Green et al., 2004). Thus, the Western Alps serves as a natural laboratory to study the interplay between dehydration, fluid flow and deformation styles of the IDEQs window, but extrapolation of these findings to fast-spreading settings should be taken with caution. We document several generations of olivine-bearing vein networks hosted in serpentinites and discuss the deformation processes that were operating during dehydration and fluid circulation within a deeply subducted slab. We document the occurrence of cyclic dilational, hybrid mode dilational-shear, as well as mineral precipitation associated with shearing, interpreted to represent localized shearing and brittle fracturing in a ductile matrix at conditions where IDEQs occur. These structures and deformation mechanisms are then compared with published data on IDEQs source properties and related experimental results. We synthesize these results and comparisons and use them to propose a large-scale model of fluid flow within the subducting oceanic lithosphere.

2. Geological Context of the Zermatt-Saas Meta Ophiolite

The Western Alps host coherent, km-thick and tens-of-km-long slivers of meta-ophiolites, extending from Voltri in Liguria (Italy), to the Zermatt and Saas-Fee region in Switzerland. These slivers constituted part of the slow-spreading Liguro-Piemontese oceanic realm, where serpentinites formed via seafloor hydrothermal alteration of the oceanic mantle, and were subducted beneath the Apulian plate (Agard, 2021; Fontana et al., 2008; Lagabrielle & Cannat, 1990; Peters et al., 2017). The serpentinized oceanic mantle that constitutes the base of these slivers has undergone eclogite-facies metamorphism and contains abundant secondary olivine veins within partially dehydrated serpentinites (Gilio et al., 2019; Hermann et al., 2000; Li et al., 2004; Plümper et al., 2017). We focus on the ZSU, which is one of these coherent slivers (e.g., Angiboust et al., 2009; Bucher et al., 2005; Dal Piaz & Ernst, 1978). The ZSU is overlaid by the Combin and Theodul Glacier Units. The former is interpreted to represent passive margin sediments, while the latter as exotic continental fragments. Both units underwent blueschist-to eclogite-facies metamorphism (Angiboust et al., 2014; Bucher et al., 2020; Negro et al., 2013). In addition, the ZSU was underthrust by the HP Monte Rosa unit, which exhibits continental affinity (e.g., Steck et al., 2015; Figures 2a and 2c).

Estimated peak pressure-temperature (P - T) conditions for the ZSU eclogites are between 2.3 and 2.5 GPa and 530–550°C (Angiboust et al., 2009), while 50–100°C warmer and (U)HP conditions were proposed for ZSU serpentinites (Li et al., 2004), as well as for subordinate sub-units such as the Lago di Cignana sliver (600°C and 3.2 GPa; Groppo et al., 2009). These peak conditions were attained at 50–44 Ma (Dragovic et al., 2020; Rubatto et al., 1998; Skora et al., 2015), followed by cooling along the epidote blueschist-facies at c. 37 Ma (Angiboust & Glodny, 2020; Reddy et al., 1999). The ZSU serpentinites exhibit widespread metamorphic veins composed of olivine + Ti-clinohumite along with diopside, chlorite and other minor phases. These ubiquitous sets of Ti-clinohumite + olivine (\pm Ti-chondrodite) veins indicate veining under (U)HP conditions at temperatures of $580 \pm 50^\circ\text{C}$ following the breakdown of brucite in the presence of antigorite (e.g., Kempf et al., 2020; see Section 5.1 for details). Furthermore, Gilio et al. (2019) suggested vein precipitation according to the dehydration reaction: primary clinopyroxene + olivine + antigorite = diopside + chlorite + Ti-clinohumite + H_2O .

Figure 2. (a) Regional map localizing the Zermatt-Saas unit (ZSU) within the Western Alps. The red stars indicate the study localities. (b) Photograph of the southern cliff of Mt. Pancherot (above Lago di Cignana lake), which represents a typical ultramafic mega-lens of the ZSU. (c) Cross-section (see panel A for the location of the transect) depicting structural relationships among the units forming the metamorphic nappe-stack in the Valtournenche area. (d) Cross-section of the lower Theodul Glacier area depicting the fabric style in the serpentinite sole and strain gradient from the glacier to the ridge. The blue stars illustrate locations within the structural profile from which the pictures were captured. (e) Photograph (extracted from Google Earth ©) showing the location and topography of the transect from panel (d).

3. Field-Scale Structures

3.1. General Observations and Previous Data

We present relevant field observations from four localities (Mt. Avic, Lago di Cignana, Valtournenche, Theodul Glacier; Figure 2a), with emphasis on the lower Theodul Glacier area (Zermatt region). The serpentine bodies occur as continuous masses mostly located at the base of the ZSU (Figures 2b and 2c). These slivers or megalenses can be traced for several kilometers along strike. Some of the mega-lenses are hosted within eclogite-facies metabasites and metasediments (e.g., Figure 2b), which display an exhumation-related blueschist-facies overprint (Angiboust et al., 2009). Rodingites, that might represent highly metasomatized former mafic dikes, are found within the serpentinite bodies (Figure 2d).

The ZSU serpentinites locally exhibit bastite (orthopyroxene pseudomorph now replaced by serpentine)-bearing levels and mineral segregations likely inherited from seafloor hydrothermal and magmatic activity, respectively (Kempf et al., 2020; Li et al., 2004). An early foliation (S1) is defined by aligned antigorite and magnetite along with veins containing metamorphic olivine and Ti-clinohumite (Li et al., 2004). This S1 fabric was transposed during the regional event that produced the main penetrative foliation S2 (Luoni et al., 2019), the latter is consistent with the regional nappe stack trend, dipping 20–40° to the NW. The main foliation S2 is defined by high-strain serpentinite (see below) displaying an anastomosing mylonitic fabric, isoclinal folds, S-C planes and stretched magnetite, antigorite, olivine, diopside and Ti-clinohumite blasts and trails. In addition, transposed, dismembered and rotated olivine-rich and Ti-clinohumite-bearing (\pm Ti-chondrodite) veins are systematically observed (Gilio et al., 2019; Kempf et al., 2020; Li et al., 2004; Luoni et al., 2018). Similar veins also occur crosscutting the S2 fabric as observed in Valtournanche (Luoni et al., 2019) and Mt. Avic localities. The S2 foliation in serpentinites is locally crenulated, defining the S3 fabric, which locally exhibits another generation of antigorite and chlorite (Li et al., 2004). The last deformation stage is a set of late subvertical fractures coated with carbonates and light green chrysotile and/or lizardite (S4; Luoni et al., 2019).

3.2. Outcrop-Scale Vein Distributions and Relationships to Strain Gradients

The strain distribution and spatial organization of S1–S3 fabrics are heterogeneously distributed within the ZSU serpentinite bodies, defining low- and high-strain domains for each fabric, as documented below and summarized in Table 1.

The recent retreat of the Theodul Glacier exposes outstanding rock outcrops, offering an exceptional opportunity to document the structural relationships among the veins and the various deformation events at the hundreds of meters-scale. The intensity of strain increases toward the major lithological contact at the boundary between the Theodul Glacier and Zermatt-Saas units, at higher structural levels with respect to the latter. This structural variation represents a progressive evolution from a low-strain region at the Theodul Glacier bed, grading upwards to a strong penetrative and anastomosing mylonitic foliation (bottom to top of the exposed cliff; Figures 2d and 2e). In the lower-strain domain, the early prograde-to-peak eclogite-facies (prograde burial) sub-vertical foliation S1 is preserved. This foliation is crosscut by syn-to-post kinematic (post S1 but pre S2) olivine + Ti-clinohumite veins, and is folded with fold axial planes parallel to the S2 regional foliation (Figure 3a). Fragments of former dilational antigorite veins display offset and domino-type boudinage in which the shear bands that accommodate deformation within vein fragments are systematically coated with olivine and oriented at moderate angles to the foliation (Figure 3b). Clasts of low-strain serpentinite also occur wrapped by sheared olivine-rich shear bands and are closely associated with veins filling the dilational sites within the clasts and the serpentinite around (Figure 3c). Likewise, metarodingites and Ti-clinohumite-bearing veins were also dragged and incorporated within localized shear bands (e.g., Figure 3d).

In the cross-section (Figures 2d and 2e), it is qualitatively shown that the ratio of undeformed veins (Type (i) and (ii)) relative to sheared veins (Type (iii)) decreases from nearly 80% to <5% in less than 50 m upwards. At the upper section of the Gandeggghütte-Theodul Glacier transect (Figure 2e), most Olivine + Ti-clinohumite metamorphic veins were transposed, smeared and affected by later-stage crenulation (Figure 3e). At the highest structural levels between the Gandeggghütte and the contact with the Theodul Glacier Unit (northwestward of the transect shown in Figure 2d), complex intercalations between low- and high-strain domains occur and are capped by ophicarbonates and a metasedimentary cover. Notably, no olivine veins are preserved at the contact with the Theodul Glacier Unit. The proportion of sheared veins within the serpentinite body increases again toward the

Table 1

Summary of the Main Structures and Deformation Features in the Context of the Metamorphic Evolution of the Zermatt-Saas Unit Serpentinites

Diagnostic structures	Illustration	P-T context
<p>Foliation S1 (Dn)</p> <p>The foliation S1 is defined by antigorite, trails of stretched magnetite, and aggregates of olivine and Ti-dinohumite. In low-strain domains, there is a preferential preservation of Type (i) and (ii) veins, as well as igneous features such as bastites and metarodigites</p>		
<p>Foliation S1 to S2 (Dn+1)</p> <p>In low-strain domains, the main foliation S2 develops within localized shear bands that cross-cut S1. Previous veins are smeared and boudinaged (Type (iii) veins), with necks filled by olivine and Ti-dinohumite. Shear bands coated with olivine accommodate deformation, leading to domino-type boudinage and angular clasts. Former igneous dikes and prograde metamorphic veins are dragged and partially incorporated into the shear bands</p>		
<p>In high-strain domains, the S1 foliation is transposed into the main foliation S2, associated with tight folding of olivine-bearing veins. The foliation spacing evolves from weak and discontinuous to penetrative</p>		
<p>Foliation S2 (Dn+2)</p> <p>Pervasive S-C-C' mylonitic foliation defined by antigorite with trails of magnetite, diopside, olivine and Ti-clinohumite in the S planes, and C' shear bands coated with olivine. Low-strain serpentinite phacoids are wrapped by the S2 foliation. Most veins and metarodigites are heavily transposed, with strain shadows and boudin necks filled by olivine and Ti-dinohumite. Type(iii) veins display mineral lineations with newly formed grains. Type (i) veins cross-cutting the S2 fabric are locally observed.</p>		
<p>Foliation S3 (Dn+3)</p> <p>Tight folding of the previous serpentinite and vein foliations and development of the S3 crenulation fabric. The S3 foliation is defined by newly formed chlorite and antigorite.</p>		

Note. The P-T grid (iii) is modified from Kempf et al. (2020).

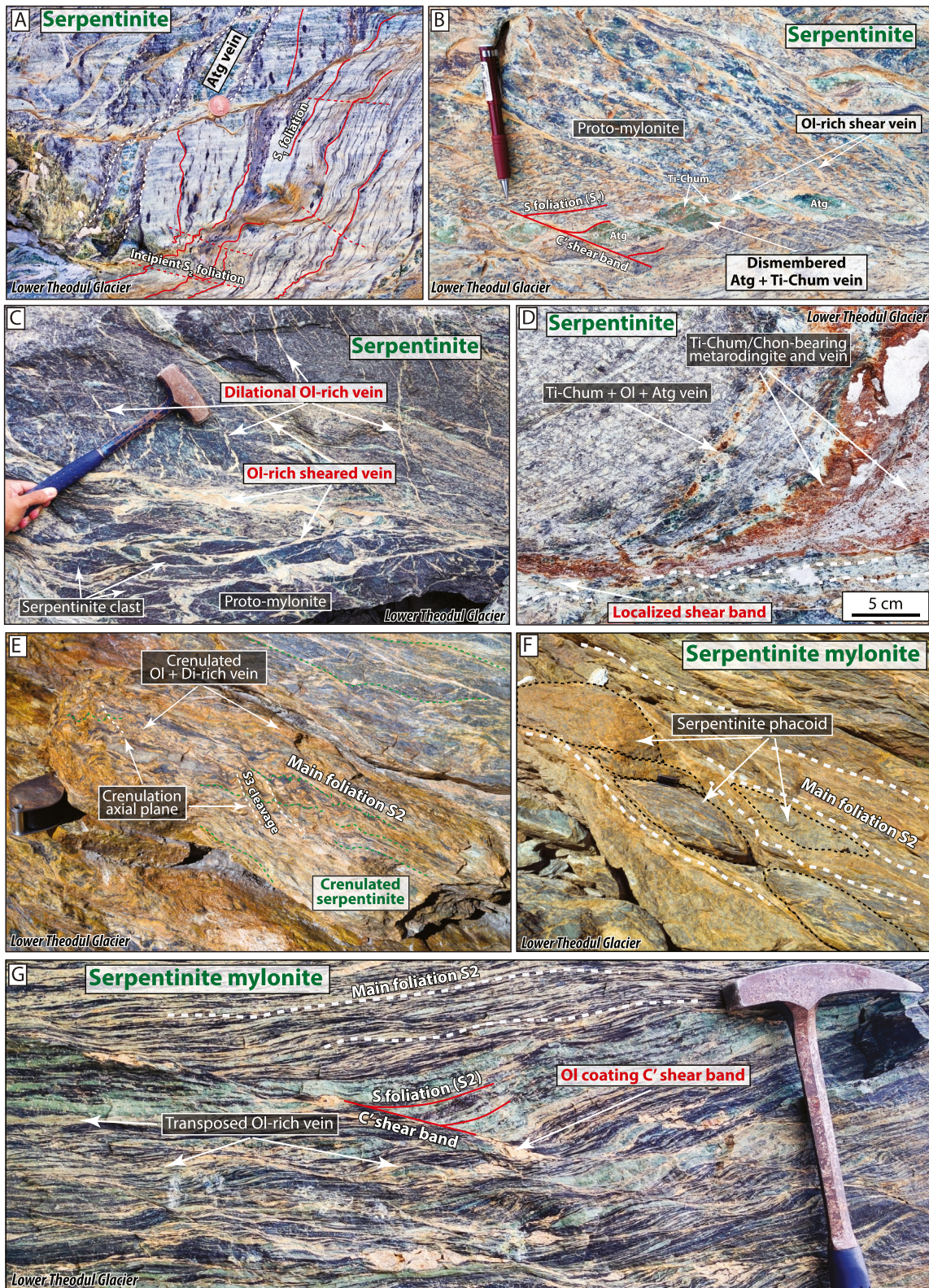


Figure 3.

contact with the underlying Monte Rosa nappe, as visible in the Gornegrat locality. Despite our best efforts, the glacier cover of the Alpine terrain did not allow us to image the strain distribution at its lower boundary. Thus, shear-related vein fabrics dominate toward the “outer” part of the ultramafic slivers whereas low-strain veins are more abundant toward their “core” (see Figure 2d for an example). This structural feature is also observable in poorly strained serpentinite phacoides embedded within a sheared serpentinite matrix (Figure 3f). Thus, the low-strain domains likely represent decimeter to hectometers-scale phacoides/lenses wrapped by the regional S2 foliation. Furthermore, rodingites are only partially affected by the deformation event leading to the S1 foliation at the glacier bed, but underwent complete transposition, boudinage and smearing along the main foliation S2 (see Figure 2d).

3.3. Metamorphic Vein Systems and the Serpentinite Host

3.3.1. Serpentinite Host Around Vein Systems

Sheared vein and monomineralic shear band structures are closely associated with or hosted within (proto)mylonitic serpentinite (Figures 3a–3d, 4a, and 4b). The (proto)mylonite displays several tens of centimeters-to millimeters long phacoids with long axes elongated parallel to the main foliation (e.g., Figures 3b and 3c). In the most strained domains (toward the top of the structural pile), the mylonite phacoids display higher aspect ratios; they can be as long as a few meters and are mostly made of moderately to weakly strained serpentinites (e.g., Figure 3f), or locally of partially serpentinitized, clinopyroxene-rich metaperidotites (Figure S1a in Supporting Information S1). The inter-phacoids space is decorated with olivine-bearing sheared veins and bands (Figures 3b, 3c, and 3f). Serpentinite mylonites exhibit S-C-C' structures characterized by an S foliation composed of serpentinite and transposed veins and C' surfaces coated with olivine-bearing shear bands (Figure 3g). We also document serpentinites with an apparently brecciated fabric characterized by angular to rounded fragments composed of weakly strained serpentinites or metaperidotites (e.g., Figure 4a and Figure S1a in Supporting Information S1).

3.3.2. Definition of the Different Vein and Shear Band Sets

Olivine-rich veins are ubiquitous among all studied localities. These veins contain one or more of: olivine, diopside, antigorite, Ti-clinohumite, chlorite, magnetite and locally Ti-chondrodite (e.g., Gilio et al., 2019; Kempf et al., 2020). We distinguish three main vein types (e.g., type (i), type (ii), and type (iii)) on the basis of field and microscale observations. Type (i) veins are observed primarily associated with the S1 fabric in low-strain domains where the S2 is not well developed. They typically sharply cross-cut the S1 foliation at low- to high-angles (Figures 4a–4c) and locally cross-cut the S2 foliation (Figure 4d). These veins are dilational and commonly form distributed networks with multiple cross-cutting sets and mutual terminations. In some places they occur in more organized en echelon arrays (e.g., Figure 4d and Figure S1b in Supporting Information S1). Vein width typically ranges from millimeters up to tens of centimeters. The vein interiors contain a range of mineral fills, including coarse blocky crystals of olivine, Ti-clinohumite and magnetite along with fibrous/tabular diopside and locally Ti-chondrodite. Some veins show evidence for multiple generations of vein opening in the form of sharp mineral zonations from center to margin: for example, in Figure 4c it is shown an antigorite vein hosting a subsequent generation of Ti-clinohumite vein precipitated at the center of the vein volume. Furthermore, in low-strain domains, intricate patterns of (sub)millimetric veinlets appear to connect or branch into strain-free, preferentially oriented millimeters-wide veins (e.g., Figures 4e and 4f). These millimeters-scale networks are analog to vein systems documented in Erro-Tobio (Ligurian Alps, Italy; Hermann et al., 2000) and interpreted as dehydration veins (Plümper et al., 2017).

Figure 3. Field photographs of low-strain (a) to (d) and high-strain (e) to (g) domain structures. (a) Serpentinite and pyroxenite segregations crenulated, overprinting the foliation S1 and defining an incipient development of the foliation S2. (b) Former antigorite + Ti-clinohumite dilational vein boudinaged in a domino-type manner, note the shear bands accommodating deformation are composed of olivine in a matrix of serpentinite. (c) Low-strain, massive serpentinite and phacoides wrapped by foliated olivine sheared veins and shear bands. (d) Ti-clinohumite ± Ti-chondrodite bearing veins and metaroddingite dikes dragged into highly localized shear bands. Note the increased development of serpentinite foliation approaching the shear band. (e) Crenulated serpentinite main foliation S2 defining the S3 foliation fabric. (f) Penetrative main foliation S2 preserving low-strain serpentinite phacoides. (g) S-C' mylonitic serpentinite in which the C' shear planes are preferentially coated with olivine. Ti-Chum, Ti-clinohumite; Ti-Chon, Ti-chondrodite.

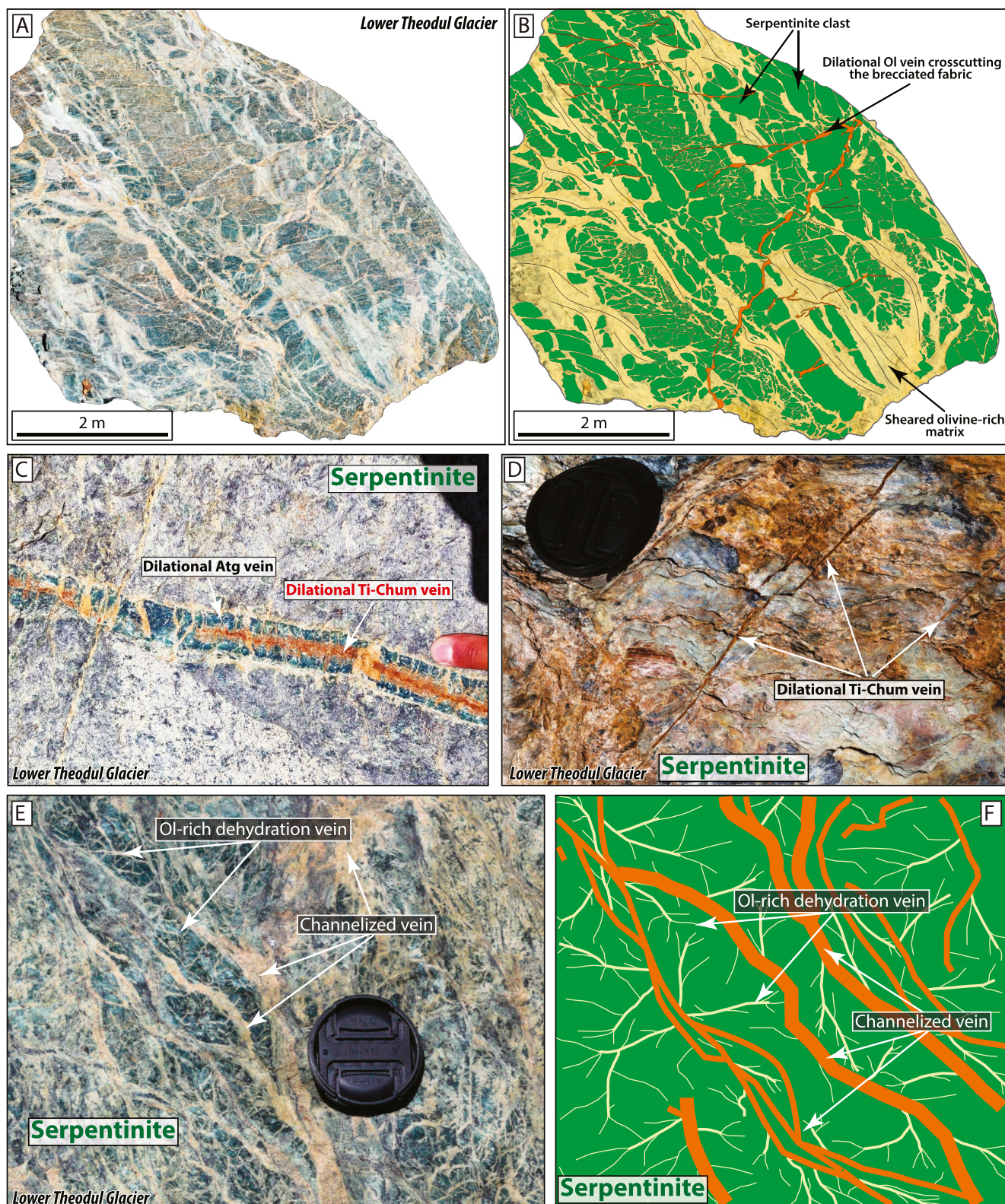


Figure 4. (a and b) Orthomosaic images and (c–e) field photographs. (a) Block next to the glacial bed showing olivine-rich veins in low-strain domains. (b) Sketch of panel (a) highlighting the main structural relationships between the different generations of veins and the serpentinite host. (c) Antigorite vein cutting across low-strain serpentinite. Note the occurrence of another generation of Ti-clinohumite veining precipitated at the center of the previous vein. (d) Ti-clinohumite-bearing veins cutting the main foliation S2. (e) Low-strain serpentinite and intricate vein networks. (f) Simplified sketch of panel (e).

Type (ii) veins co-occur with type (i) veins but are distinguished because they show evidence for rotational shear during emplacement. These veins form sets of conjugated networks as well as offsetting serpentinites fragments and sheared veins (Figures 4a and 4b; see below). Type (iii) veins correspond to highly strained and shear-dominated structures characterized by centimeter-long fragmented and rotated porphyroclasts in a sub-millimetric matrix (Figure 5a and Figure S1c and S1d in Supporting Information S1). These sheared domains and veins are oriented parallel or at low-angles to the main foliation with the lineation trending NE to SE (see rose diagram in Figure S2 in Supporting Information S1), locally displaying small step-overs (Figure 5b). They are crosscut by Type (i) veins, incorporated as rotated clasts within sheared domains (e.g., Figures 4a, 4b, and 5c; Figure S1d in Supporting Information S1) or folded (Figure S1e in Supporting Information S1). These structures also develop horsetail splay geometries (Figures 5d and 5e). Type (iii) veins also show evidence for new mineral growth during transposition (see below), with the lineation defined by elongated Ti-clinohumite, diopside and olivine and are systematically found in all studied localities (Figures and S1c and S2 in Supporting Information S1). Dilatational jogs, filled with Ti-clinohumite (Figure 5f), olivine and/or diopside were also observed.

3.3.3. Overview of the Main Veining Stages

For the sake of clarity, we provide a brief interpretation of the various olivine-rich vein types identified in our study (see Section 5.2 for further details). Type (i) veins are inferred to have formed due to dilatational fracturing and mineral precipitation, and are henceforth denoted as dilatational veins throughout the text, whereas Type (ii) veins are interpreted as mode II dilatational-shear veins. Type (iii) structures correspond to brittle-ductile shear bands that represent transposed and rotated veins of type (i) and (ii), alongside newly formed mineral phases.

A block located at the Theodul Glacier bed, representing the low-strain domain, is used to illustrate different deformation-veining stages (Figures 4a and 4b). The primary structural features are poorly foliated serpentinite fragments, which exhibit angular morphologies. These fragments develop crackle or mosaic-type breccia (in the sense of Woodcock & Mort, 2008) fabric and domino-type dismembering (Figure 4a). The inter-clast space within the breccia is filled with olivine-rich veins. These veins formed in multiple stages, exhibiting mutual crosscutting relationships summarized as follows:

1. Dilatational and conjugate vein sets preserved within serpentinite clasts.
2. Olivine veins (type (iii) veins) produced during and affected by shearing. These structures accommodated the majority of strain around and within the serpentinite clasts, commonly transecting or transposing the previous dilatational veins.
3. Dilatational and dilatational-shear veins crosscut all previous structures, including the serpentinite clasts and the sheared-olivine vein matrix. Note that some dilatational veins developed during stage (iii) are embedded, deformed, and incorporated within the sheared veins.

Similar features were observed in the Lago di Cignana locality, where some fragments bear extensional and sheared veins, while Ti-clinohumite- and olivine-bearing vein fragments are also found as clasts (Figure S1a in Supporting Information S1). We emphasize the occurrence of pristine to slightly deformed Ti-clinohumite- and olivine-bearing dilatational veins cutting across the brecciated fabric (Figure S1a in Supporting Information S1).

4. Microstructures and Textures

Petrographic and microstructural observations in the variety of vein systems and host serpentinite are presented in a set of 12 samples (see Table S1 in Supporting Information S1 for sample coordinates). The samples were sectioned normal to the main foliation and parallel to the lineation. Full details on the parameters and the analytical techniques used in this study are provided in the supplementary material.

4.1. Serpentinite (proto)mylonites and Breccia

The serpentinite host surrounding sheared veins commonly displays a (proto)mylonitic or brecciated fabric composed of sigmoidal to angular fragments and/or porphyroclasts of olivine, diopside and pseudomorphs after clinopyroxene within a fine-grained matrix of antigorite (Figures S3e and S3f in Supporting Information S1). Low-strain serpentinite are weakly foliated, massive serpentinites displaying mesh textures (Figure 6a) characterized by relatively randomly oriented laths of antigorite. At the contact with highly sheared veins, the foliation is locally more developed (e.g., Figure 7b). High-strain serpentinites are characterized by strongly foliated, fine-

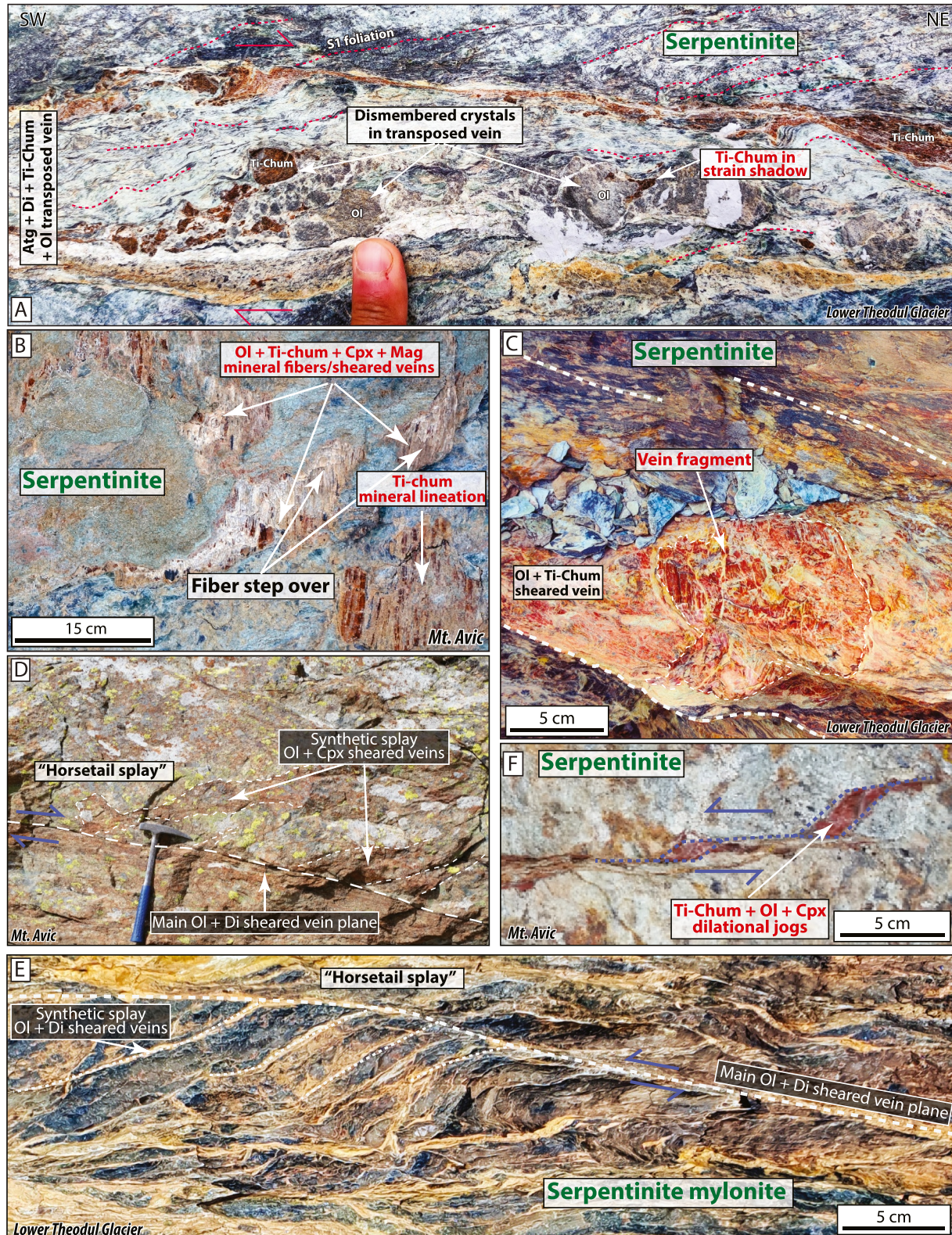


Figure 5.

grained antigorite wrapping around coarser-grained, low-strain antigorite aggregates along with metamorphic olivine and diopside porphyroclasts, producing the anastomosing main foliation S2 (Figure 6b and Figure S3j in Supporting Information S1). In the most deformed serpentinite mylonites, no low-strain features are preserved, developing a pervasive foliation with a grain size smaller than the previous fabric (Figure 6c). The anastomosing foliation is also composed of stripes of tabular diopside grains elongated parallel to the main foliation, fine-grained olivine aggregates, and Ti-clinohumite porphyroclasts surrounded by pressure shadows containing olivine (Figure 6d). In mylonitic serpentinites, olivine shear bands coat S-C' planes. We identified at least two generations of antigorite based on variations in the Al content of these sigmoidal domains, in which Al-richer is surrounded by Al-poorer antigorite (Figure 6e).

4.2. Dilational (Type I) Veins

Dilational veins contain blocky crystals, with sizes ranging from millimeters to several centimeters (locally up to tens of centimeters), and are generally composed of olivine (>50 vol%), diopside, Ti-clinohumite, and magnetite (e.g., Figure 7a). These veins are millimeter to tens of centimeter-wide and display sharp or planar to curvy-planar host vein margins (Figures 7a and 7b). The strain-free blocky crystals in these veins are sharply faceted (e.g., Figure 7a), while antigorite, diopside and locally olivine crystals occur elongated perpendicular to the host-vein walls (Figures 7b and 8a).

4.3. Sheared (Type III) Veins and Shear Bands

The transition from dilational to sheared veins and shear bands is illustrated in Figures 7a and 7c. There, a dilational (type i) vein exhibits slight bending of the grains as they approach the vein margins (see the red arrow in Figure 7a). With progressive strain, these dilational veins eventually develop fine-grained, localized shear bands (Figures 7b, 7c, 8a, and 8b). Note that in massive serpentinites (e.g., poorly foliated), the sheared veins sharply transect the serpentinite host as well as previous dilational veins developing sharp and planar host vein margins (Figure 7b).

Highly strained veins (Figures 7d and 8c) display a mylonitic fabric composed of olivine + Ti-clinohumite ± diopside porphyroclasts. The porphyroclasts are generally equidimensional and (sub)rounded to angular in shape, with some exhibiting elongation along the main stretching direction and mild undulose extinction. Within sheared veins, diopside defines two microfabric types that are recognized on the basis of their grain size and shape, including (a) bimodal-type and (b) equigranular-type domains. Sheared veins containing bimodal grain size distributions (bimodal-type) are characterized by elongated tabular diopside grains with diameters of several hundreds of microns, where the smaller grains (<100 μm) surround the porphyroclasts or occur within boudin necks. Both grain size populations exhibit a shape preferred orientation which defines the macroscopic lineation. The second diopside microfabric (equigranular-type) is characterized by equigranular grains, mostly below 100 μm in diameter and elongated-tabular crystal shapes. While the occurrence of both bimodal- and equigranular-type fabrics in a single sample is rare, the equigranular-type fabric dominates. In addition, rare chlorite and antigorite boudins (Figure 7d and Figure S3a–S3d in Supporting Information S1) with olivine- and/or diopside-filled necks are observed (Figures S3d and S3e in Supporting Information S1).

Fine-grained Ti-clinohumite crystals with different orientations, as inferred from extinction angles, envelope larger Ti-clinohumite porphyroclasts developing strain shadows (Figures 7d and 8c; see also Figures S3h and S3i in Supporting Information S1). Likewise, large Ti-clinohumite crystals are boudinaged with boudin necks filled with prismatic-tabular Ti-clinohumite and diopside grains elongated perpendicular to the margins of the porphyroclasts (Figure 8c). In addition, dusty (inclusion-rich) Ti-clinohumite porphyroclasts are rimmed by another generation of clean (inclusion-free) Ti-clinohumite (Figure S3i in Supporting Information S1). Similar microstructures are observed in olivine, where porphyroclasts are surrounded by another generation of elongated olivine grains (Figure 8d). Note that these olivine porphyroclasts display weak undulose extinction (Figure 8d).

Figure 5. Field photographs of shear structures. (a) Field image of a sheared vein composed of olivine and Ti-clinohumite porphyroclasts in a fine-grained matrix of antigorite and diopside, displaying sharp contact with the host serpentinite and top to the NE shear sense. (b) Olivine, diopside and Ti-clinohumite-bearing mineral fibers and lineations, view normal to the XY-plane of the strain ellipsoid. (c) Sheared vein in high-strain serpentinite hosting a fragment of a Ti-clinohumite-bearing vein, which also displays a mineral lineation. (d) Geometrical relationship between a main olivine-coated fault plane and the adjacent conjugate fault systems, developing a horsetail splay. (e) High-strain serpentinite developing horsetail splays at the millimeters-scale. (f) Ti-clinohumite-filled dilational jog in serpentinite.

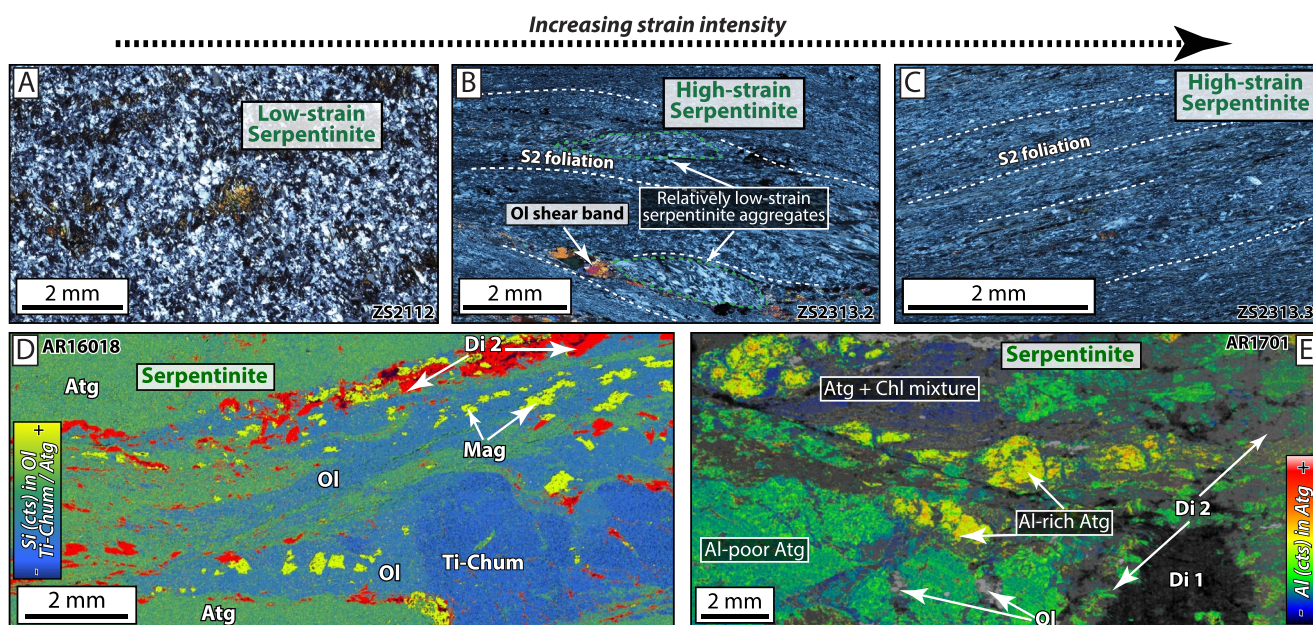


Figure 6. (a–c) Cross-polarized light photomicrographs and (d and e) phase masks based on EDS X-Ray maps. (a) Low-strain serpentinite displaying randomly oriented antigorite laths with a weak foliation. (b) High-strain serpentinite mylonite. Note the occurrence of relatively low-strain domains. (c) High-strain serpentinite displaying very fine-grained grains. (d) Si content in Olivine, Ti-clinohumite and antigorite overlaid by a phase mask image highlighting clinopyroxene and magnetite. (e) Al content in antigorite from a mylonitic serpentinite host.

Furthermore, large Ti-clinohumite porphyroclasts are rotated and display twins (Figure 8e). Sharply truncated crystal surfaces along with euhedral and blocky grains surround the larger porphyroclasts (Figure 8c). Diopside, along with subordinate olivine, Ti-clinohumite, antigorite and magnetite (Figures 7d and 7f) define the lineation and foliation in the fine-grained matrix and exhibit fibro-tabular shape. In sheared veins, diopside-rich aggregates contain highly angular grains, along with offset and broken crystals surrounded by a fine-grained, fibrous matrix resembling a cataclastic fabric (Figure 7e).

5. Discussion

5.1. Veining Sequence at (U)HP Conditions

The presence of olivine, diopside and Ti-clinohumite-bearing veins exposed in the Alpine meta-ophiolitic ZSU offers a valuable opportunity to document dehydration processes within the eclogite-facies oceanic mantle. Thermodynamic modeling, based on the temperature dependence of Al in antigorite and olivine (e.g., higher Al indicating elevated temperatures; Padrón-Navarta et al., 2013), points to peak temperatures of 520–650°C, suggesting that the antigorite + brucite dehydration reaction was responsible for generating these veins (Kempf et al., 2020). This temperature range is supported by the absence of orthopyroxene, which is expected to form at temperatures above 650°C (Padrón-Navarta et al., 2011; Scambelluri et al., 2014). Moreover, the occurrence of Ti-clinohumite and Ti-chondrodite indicates peak pressures above 1.6 GPa (Shen et al., 2015), most likely between 2.3 and 2.7 GPa, consistent with estimations from Zermatt, Valtournanche, Lago di Cignana, and Mt. Avic (Gilio et al., 2019; Li et al., 2004; Luoni et al., 2018; see also López Sánchez-Vizcaíno et al. (2005)). These *P-T* conditions align with those calculated for eclogites and metasediments along the ZSU (Angiboust et al., 2009; Bucher et al., 2005; de Meyer et al., 2014) confirming that the veining sequence occurred during the same tectono-metamorphic event.

By integrating these petrologic studies with structural characterization, we provide new insights into the deformation stages and fabric evolution during burial and exhumation (see summary Table 1). The early stage involved dilational veining crosscutting a low-strain serpentinite, exhibiting dilational veining patterns (Figures 4a and 4b). These veins were first filled with antigorite (see Kempf et al. (2020) for details), and were subsequently re-opened and re-filled with Ti-clinohumite and olivine. These parageneses suggest that early veining initiated in the antigorite stability field at temperatures between 400 and 460°C (Schwartz et al., 2013; Trommsdorff &

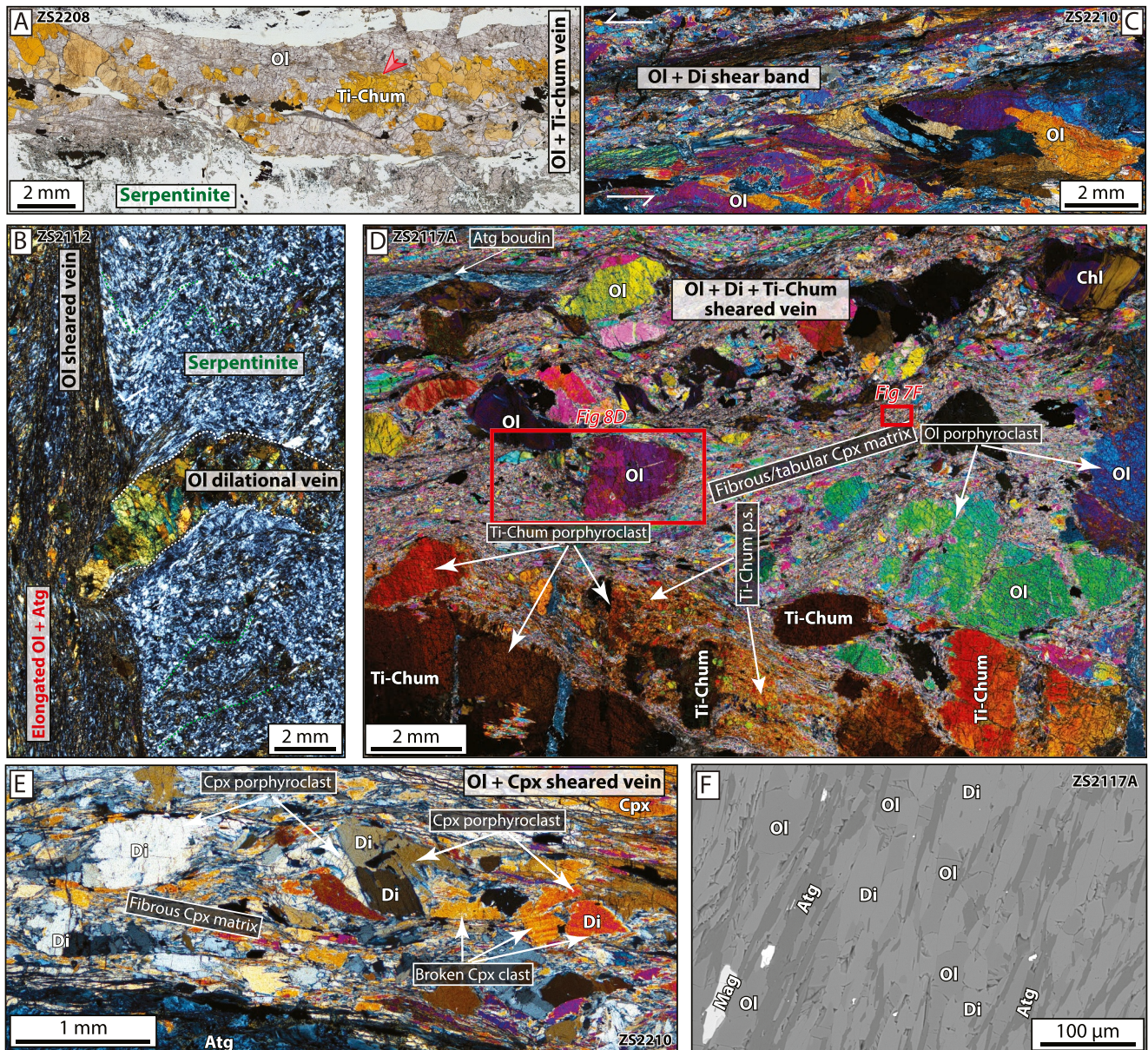


Figure 7. (a) Plane-polarized and (b–e) cross-polarized light photomicrographs and backscattered electron image (f). (a) Dilational olivine and Ti-clinohumite vein in serpentinite displaying euhedral blocky crystals as well as sharp host-vein walls contact. The red arrow indicates slight bending of grains. (b) Fine-grained sheared vein composed of olivine + antigorite sharply transecting a low-strain serpentinite along with a dilational olivine vein, the latter showing elongated olivine crystals oriented perpendicular to the host-vein walls. (c) Former dilational vein displaying elongated and bent olivine and diopside crystals evolving toward a localized shear band involving strong grain size comminution. (d) General fabric of a sheared vein containing olivine and Ti-clinohumite porphyroclasts with sigmoidal to highly angular morphologies in a matrix of foliated fibrous/tabular diopside. Note the occurrence of fine-grained Ti-clinohumite grains in pressure shadows around larger clasts. (e) p. s., pressure shadow. Sheared vein containing highly angular, brittlely fractured diopside clasts in a matrix of fibrous/tabular grains. (f) Inset of panel D showing the fine grained matrix, note the fibrous/tabular habit of olivine and diopside. See Figures S3a and S3b in Supporting Information S1 thin-section photo mosaic locating panel (d).

Evans, 1980) but occurred predominantly at conditions around 550–600°C (60–80 km depth) within the stability field of metamorphic olivine (Kempf et al., 2020). These dilational veins were sheared and incorporated into sheared veins that define the S1 or the incipient S2 foliation (Table 1). These sheared veins were crosscut by subsequent generations of dilational (+dilational-shear) veins (stages (i) and (ii)), suggesting cyclic dilational (and dilational-shear) veining with localized shearing (stage (iii)) during burial up to near-peak conditions.

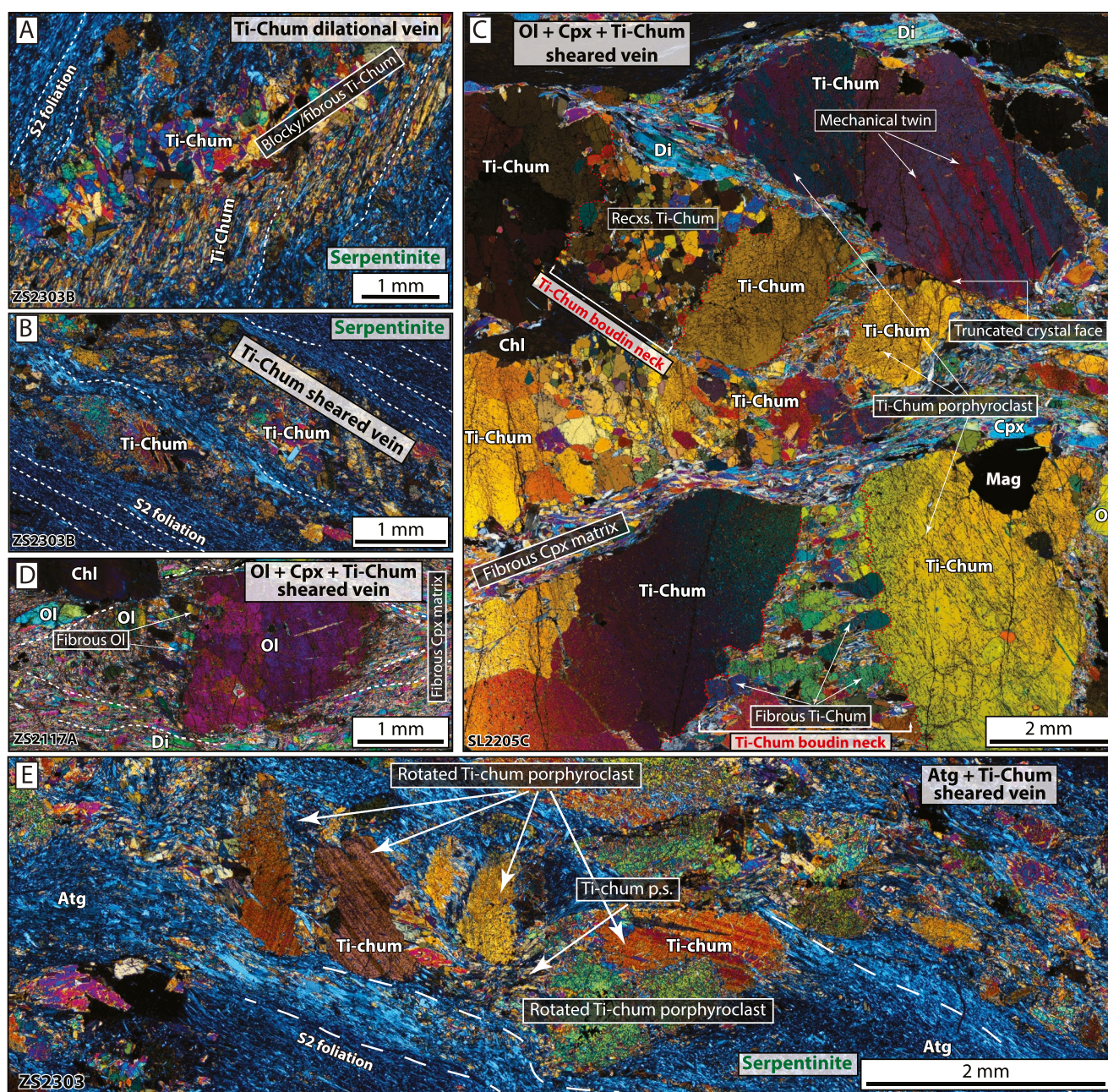


Figure 8. Cross-polarized light photomicrographs of sheared veins and serpentinite host. (a) Blocky and fibrous crystals of Ti-clinohumite in a former dilational, now partially transposed vein along with elongated crystals oriented according to the main foliation. (b) Transposed Ti-clinohumite vein. Some blocky and elongated crystals occur as relics from the former dilational structures, indicating vein transposition accompanied by crystal rotation. (c) Ti-clinohumite porphyroclasts embedded in a matrix of fibrous/tabular diopside displaying crystals that have been torn apart. The interclast space is filled with Ti-clinohumite and diopside fibers oriented perpendicular to the margin of the porphyroclast. In addition, other torn-apart crystals contain equigranular and blocky Ti-clinohumite filling. Note the occurrence of mechanical twins and sharply transected crystal faces in some large Ti-clinohumite porphyroclasts. (d) Inset of Figure 7d depicting fibers of olivine around olivine torn apart crystals. (e) Serpentinite hosting partially transposed Ti-clinohumite-bearing veins along with rotated porphyroclasts and newly grown Ti-clinohumite fibro/tabular grains. Recxs, recrystallized; p.s., pressure shadow.

These structures were then heavily transposed and smeared leading to the main foliation S2. Notably, the mylonitic fabric S2 is transected by Ti-clinohumite- and olivine-bearing dilational veins (e.g., Figure 4d and Figure S1a in Supporting Information S1; see Luoni et al., 2019 for similar observations in Valtourneche), as well as C' shear bands coated with olivine (Figure 3g), along with Ti-clinohumite and olivine-bearing fibers representing incremental growth in the stretching direction (Figure 5b and Figure S2 in Supporting

Information S1). In addition, the mylonitic foliation, characterized by antigorite bearing higher aluminum contents within cores (Figure 6e), indicates at least two stages of fabric development starting at near-peak (U)HP conditions and evolving during cooling (Padrón-Navarta et al., 2013). The main foliation S2 of the Western Alps serpentinites is classically attributed to exhumation-related shearing along the subduction environment (Luoni et al., 2019). Thus, the occurrence of (U)HP minerals in these structural domains suggest the development of the mylonitic fabric during the earliest stages of exhumation when the slivers conforming the ZSU were still subject to (U)HP conditions, before re-equilibrating later under blueschist to greenschist-facies conditions (Table 1). Lastly, all of these structures were overprinted by the S3 crenulation cleavage and S4 structures, likely forming during later-stage, exhumation-related regional backthrusting during collisional processes (Luoni et al., 2019).

5.2. Interpretation of Structures and Microstructures

5.2.1. Dilational Veining at (U)HP Conditions

The mechanical implications of serpentinite dehydration remains debated because it is unclear whether conditions of near-lithostatic or fluid overpressures capable of inducing weakening or shearing are attained (e.g., Chernak & Hirth, 2011; Clément et al., 2019; Davies, 1999; Dobson et al., 2002; Ferrand et al., 2017; Jung & Green, 2004; Jung et al., 2004; Perrillat et al., 2005; Plümper et al., 2017). The absence of fluid overpressures is attributed to the gradual increase in the Clausius-Clapeyron slope with pressure and the resultant negative volume change at pressures exceeding c. 2.5 GPa (Bose & Navrotsky, 1998; Ulmer & Trommsdorff, 1995). This process could promote porosity development, although this is likely of minimal magnitude due to the negligible net volume change of the brucite-out reaction under these conditions (very steep Clausius-Clapeyron slope). If permeability is increased, it can also facilitate fluid drainage, thereby hindering fluid accumulation and overpressures (Plümper et al., 2017). Therefore, some of the few existing studies interpreted (U)HP olivine veins as resulting from static and reaction-induced “veining,” without involving deformation, shearing, and/or fluid overpressure-related fracturing (Huber et al., 2022; Plümper et al., 2017).

We stress that a substantial amount of veins exhibit features consistent with transient fluid pressure accumulation potentially exceeding lithostatic levels and subsequent dilational fracturing (e.g., Davies, 1999; Dobson et al., 2002) as well as the presence of free fluids. Those include (a) dilational veins and jogs (Figure 5f); (b) sharp host-vein walls and en échelon arrays (Figures 4a, 7a, and 7b; Figure S1b in Supporting Information S1); (c) blocky, euhedral and centimeter-sized crystals in veins (Figures 7a, 7b, 8a, and 8c); (d) fibrous crystals in veins indicating syntaxial/antitaxial growth (Figure 7b); (e) mutual cross-cutting relationships between various veining and shearing events (e.g., Figures 3b and 3d; see below). Discrepancies between natural observations and previous experimental and numerical investigations may arise from local variations in bulk rock composition, rock fabric heterogeneity or the injection of external fluids. In the first case, local fluid pressure perturbations involving pressure drops below the brucite-out reaction boundary have been invoked to explain uneven dehydration patterns in (U)HP serpentinites, resulting in heterogeneous olivine formation (Schmalholz et al., 2023). However, it is more likely that local chemical variations within the bulk rock volume play a significant role. Variable Si:Mg ratios resulting from pre-subduction serpentinitization processes (low Si:Mg generates more brucite), as evidenced from serpentinitized MOR peridotites (Klein et al., 2020; Malvoisin, 2015), can lead to different amounts of brucite and, consequently, varying rates of H₂O production at depths (e.g., Huber et al., 2022; Kempf et al., 2020). In the second scenario, the absence of a strong serpentinite fabric in low-strain domains could create less permeable domains conducive to fluid accumulation (Gasc et al., 2017). Conversely, strongly foliated antigorite schists would favor foliation-parallel fluid drainage (Hermann et al., 2000; Kawano et al., 2011). We thus hypothesize that low-strain and low Si:Mg, massive serpentinites may represent an environment prone to fluid accumulation. In the latter case, in situ $\delta^{18}\text{O}$ measurements in antigorite and olivine demonstrated disequilibrium, interpreted as representing open system and external fluid infiltration (Ulrich et al., 2024). At depths of c. 80 km, injection of externally derived fluids most likely occurs at near-, potentially supra-lithostatic pore fluid pressure conditions and permit local fracturing along the fluid path (e.g., Taetz et al., 2018).

5.2.2. The Evolution From Dilation to Brittle-Ductile Shearing

The deformation patterns observed in vein-filling minerals and shear bands offer valuable insights into the dynamic mechanisms governing vein deformation and fabric evolution subsequent to vein emplacement. We document Ti-clinohumite- and olivine-bearing mineral lineations decorating foliation-(sub)parallel vein surfaces

(Figure 5b and Figure S2 in Supporting Information S1) as well as fibers filling boudin necks (e.g., Figure 8c). These patterns suggest incremental mineral growth at (U)HP under a stressed system (see Jábaloy-Sánchez et al., 2022 for a similar example). Moreover, veins forming conjugated sets (Figure 4a) or “horse-tail” splays (Figure 5d) indicate mixed dilational-shear fracturing. The mutual cross-cutting relationships within serpentinite (proto)mylonites and/or breccias containing clasts of vein-hosting serpentinite, along with dilational veins cross-cutting these structures (Figure 4a and Figure S1a in Supporting Information S1), suggest cyclic brittle failure within an otherwise viscous environment.

Furthermore, the associated olivine, Ti-clinohumite and diopside sheared veins and shear bands exhibit a porphyroclastic fabric within a matrix of foliated fibrous/tabular diopside (e.g., Figure 7d). Fibrous/tabular diopside wrapping larger porphyroclasts display strong SPOs with the long axis of the crystals oriented according to the macroscopic lineation. The bimodal-type diopside fabric contains large grains surrounded by smaller grains within boudin necks along with brittlely deformed diopside aggregates (Figure 7e). This fabric is inferred to have formed due to micro-boudinage followed by mineral precipitation in the neck site. The equigranular-type fabric in diopside is then interpreted to represent a more advanced stage of recrystallization and grain size reduction subsequent to micro boudinage. Similarly, Ti-clinohumite develops mineral fibers within boudin necks and coating sheared veins, along with sharply truncated crystal surfaces (Figure 8c). In partially transposed veins, Ti-clinohumite still preserves blocky or prismatic crystal shapes (Figures 8a and 8b), but their elongation is now oblique to the host-vein walls. Olivine porphyroclasts exhibit undeformed and slightly internally deformed clasts (Figure 8d) showing elongated fibers (e.g., Bons et al., 2012) along grain boundaries, possibly representing pressure shadows. Overall, these microstructures, together with the occurrence of a new generation of Ti-clinohumite on the rims of rotated porphyroclasts (Figure 8e and Figure S3h in Supporting Information S1), suggest deformation first by mechanical rotation and micro-fracturing/cataclastic flow, followed by viscous creep and oriented mineral growth. Nevertheless, more detailed studies are needed in order to elucidate the role of crystal plasticity versus pressure-solution or diffusion creep during cyclic brittle-viscous deformation at (U)HP.

5.2.3. Olivine-Rich Veins as Mechanical Heterogeneities and Strain Localization

Considering that the vein systems represent sheared volumes composed of stiff minerals such as olivine and Ti-clinohumite in a serpentinite matrix, we conclude that the veins acted as stress heterogeneities within a viscous environment (Hermann et al., 2000; Schmalholz et al., 2023). As noted, Ti-clinohumite and diopside clasts within veins exhibit brittle features (Figure 7e), pressure-shadows (Figures 7d and 8e) and mineralized boudin necks (Figure 8c), supporting the hypothesis of an initial brittle stage followed by subsequent viscous creep (see also Bial & Trepmann, 2013; Wassmann et al., 2011). Our natural, strongly foliated antigorite schists (e.g., Figures 6b and 6c) exhibit a clear high-strain fabric, which also involved significant grain size reduction and foliation development. In contrast, low-strain serpentinite displays coarser-grained, randomly oriented laths of antigorite (e.g., Figure 6a). In the latter, this pattern potentially resulted from randomly oriented laths formed during static serpentinitization of the seafloor peridotite, reflecting the typical mesh texture of lizardite (Plümper et al., 2012). Furthermore, sharp knife-like sheared veins cut across (Figures 7b and 7c), while olivine-rich sheared veins preferentially accommodated deformation within low-strain serpentinite. We interpret these features as representing preferential and highly localized deformation, and simultaneous or subsequent viscous flow in a low-strain serpentinite matrix. These observations demonstrate that serpentinites can remain brittle at temperatures as high as $580 \pm 50^\circ\text{C}$, and aligns with experimental investigations on deformed serpentinite, which exhibit localized brittle deformation (French et al., 2019; Proctor & Hirth, 2016) and a minor strength difference between dunites and serpentinites at high pressures (Hirauchi et al., 2020). Furthermore, it supports the notion that rheological heterogeneities enhance transient, localized shearing under high-pressure conditions (Angiboust et al., 2017; Behr et al., 2018; Muñoz-Montecinos et al., 2023).

5.3. Fluid-Induced Strain Localization in the Intermediate-Depth Seismicity Window and Comparison to Geophysical Data

Field observations along the ZSU exhibit ultramafic slivers with strain gradients, enabling the documentation of the feedbacks between fluid flow and deformation. At the termination of the lower Theodul Glacier, the least strained inner domains grade toward high-strain domains at upper structural levels (Figure 2d). This observation highlights a strain gradient at the hundreds of meters-scale, in which highly sheared regions resulted from mutually overprinting fluid-enhanced brittle-ductile events. We interpret these meso- to large-scale structural and

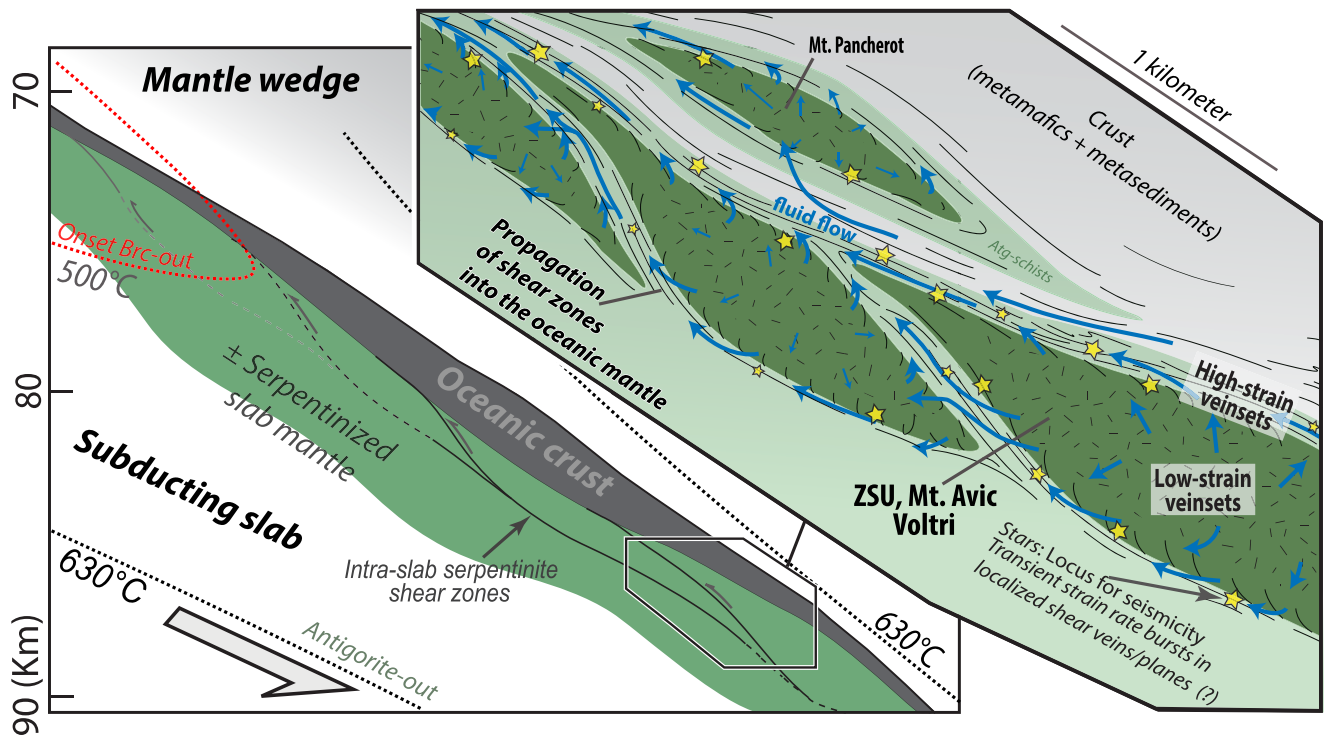


Figure 9. Conceptual sketch showing the tectonic and fluid processes during near-peak burial to early exhumation metamorphism and associated deformation along intra-slab, interface sub-parallel shear zones. Yellow stars illustrate the location of brittle-ductile events associated with high-strain domains, as recorded in the studied rocks. Low-strain veinsets are mainly found in the core of ultramafic slivers, while highly strained veinsets were mainly observed associated with broad, sheared domains wrapping the megacrysts or slivers.

crosscutting relationships as resulting from a critically unstable regime due to high pore fluid pressures (near lithostatic) as a consequence of fluid supply derived from the brucite + antigorite reaction or the injection of external fluids. While Type (i) veins most likely formed as a consequence of transient increments in pore fluid pressures, which may reach values in the order of 10 MPa (Schmalholz et al., 2023), the identification of transposed former dilational veins and newly formed shear bands (Type (iii)) suggest that brittle veins may eventually evolve into shear zones. These shear zones likely form around slivers where the ambient stress field may locally depart from the hydrostatic state (Schmalholz et al., 2023). In this model, brittle-ductile deformation is highly localized at the margins of the slivers composing the slab mantle, allowing for fluid flow along the subduction channel and perhaps to the slab-mantle wedge interface (Figure 9; e.g. McGary et al., 2014). This model is supported by geochemical data on veins and associated shear zones indicating large-scale fluid flow with mixed meta (ultra)mafic-sedimentary sources (Angiboust et al., 2014; Clarke et al., 2020; Ulrich et al., 2024). Thus, fluid circulation is envisioned as a “pulse-like” process that leads to cyclic dilational and hybrid dilational-shear fracturing and localized brittle-ductile shearing within the IDEQ source. This hypothesis aligns with experimental and field studies suggesting that fluids in sheared serpentinites may percolate via deformation-induced interconnected permeability (Angiboust et al., 2014; Auzende et al., 2015; Hermann et al., 2000). Even if a precise quantification of the fluxes is difficult to evaluate, our results suggest that within ZSU serpentinites, fracture-controlled permeability has transiently prevailed over matrix permeability during peak burial to early exhumation (e.g., Muñoz-Montecinos & Behr, 2023).

Our field and structural observations are in line with recent seismological studies imaging the IDEQs window worldwide. In northern Chile, transiently high V_p/V_s ratios (>2) in the serpentinitized lithospheric mantle are interpreted as resulting from fluid drainage into vein-like structures (fluid-filled cracks) at near-lithostatic pore pressure conditions (Bloch et al., 2018). More recently, Delbridge et al. (2024) used high-resolution waveform data associated with the Tohoku-oki Earthquake ($M_w = 9$) to constrain the physical properties of the IDEQ window in North Eastern Japan. They demonstrated that the effective stress state within the upper seismicity plane available for seismic failure is extremely low (~ 1 MPa), requiring near-lithostatic pore fluid pressure conditions.

Furthermore, thermodynamic modeling applied to the Central Mexico subduction thermal structure suggests that dehydration of the uppermost part of the serpentinized mantle could cause positive volume change-triggered fluid overpressure (Gutiérrez-Aguilar et al., 2022), thus inducing fracturing. Lastly, Craiu et al. (2022) showed that the generation of IDEQs in the Vrancea slab (Romania) down to 100–130 kms depth could be linked to preferential shearing at the margins of large-scale peridotite blocks. We stress that the range of brittle-ductile structures reported here are in line with these models, and emphasize that the combination of stress heterogeneities and near-lithostatic fluid pressure conditions enhanced localized deformation and strain accumulation at the margins of ultramafic slivers (Figure 9). However, it is worth noting that most of these geophysical studies documented processes in fast-spreading ridge settings, where the degree of serpentinization is poorly constrained (Grevemeyer et al., 2018). Therefore, our observations should also take into account the deformation mechanisms of variably serpentinized peridotites to allow more direct comparison.

At the moment, we cannot demonstrate that (sub)seismic slip rates were achieved here. Nevertheless, some of the brittle structures documented in the ZSU could have resulted from transient highs in strain rate and highly localized cataclasis or micro-fracturing, overprinted by viscous flow. In fact, switching between brittle-ductile deformation under transiently high pore fluid pressure conditions is key for the generation of slow slips and tremors within shallower subduction interfaces (e.g., Angiboust et al., 2015; Audet & Bürgmann, 2014; Behr & Bürgmann, 2021; Muñoz-Montecinos et al., 2020; Tarling et al., 2019), involving strain rate bursts at low differential stresses (Oncken et al., 2022; Shelly et al., 2006). Thus, we speculate that some of these brittle-ductile fabrics could have resulted from some of IDEQs (Brantut et al., 2017) as well as from slow slip and tremor processes (Chernak & Hirth, 2011; French et al., 2019). Nevertheless, we cannot rule out the possibility that other processes capable of producing strain rate bursts, such as post-seismic propagation of deformation toward mantle depths (Wang et al., 2020) or viscoelastic rebound due to sudden pulldown (Bedford et al., 2020), in addition to local stress perturbations during ductile shearing (Schmalholz et al., 2023), could have contributed to the finite deformation pattern recorded here.

Regardless of the specific processes, our observations underscore the capability of metamorphic fluids to trigger cyclic brittle-ductile deformation and strain localization in and around discrete olivine-rich shear volumes within the IDEQ source. Thus, challenging the classical vision of a deep serpentinized environment purely deforming in a ductile manner. Furthermore, our observations suggest that, under certain circumstances, serpentinites may develop brittle heterogeneities that persist even under (ultra)high-pressure conditions.

6. Conclusions

We identify cyclic events of brittle-ductile shearing interspersed with dilational veining associated with metamorphic vein systems formed as a consequence of prograde dehydration of serpentinites. These olivine-rich veins formed as brittle features and preferentially accommodated subsequent deformation relative to the host serpentinite, suggesting that serpentinites can remain brittle within the Intermediate Depths Seismicity region. Microstructural observations within these high-strain veins reveal that olivine and Ti-clinohumite developed boudins and porphyroclasts sealed with mineral fibers, suggesting pressure-solution or diffusion-dominated mechanisms following grain size reduction. Crosscutting relationships between veins and mylonitic/brecciated serpentinites indicate that brittle-ductile events likely occurred via strain rate bursts at near-lithostatic pore fluid pressures and low effective stress. Shear strain concentrated along the margins of ultramafic slivers, enhancing fracture-controlled permeability and fluid flow at the kilometer-scale along the deep subduction environment. The occurrence of brittle-ductile features, along with dilational veins in mutual crosscutting relationships and transient strain localization, sheds light on the potential for high strain rates within interface-parallel shear zones. Similar structural features have been imaged at the base of the deep subduction seismogenic zone and are considered to result from deformation at strain rates associated with (sub)seismic activity. Therefore, we speculate that some of the documented fabrics are the result of deformation processes occurring at strain rates faster than those typically associated with plate convergence velocities, perhaps reaching (sub)seismic levels.

Data Availability Statement

Raw files for EDS X-ray maps, as well as processed drone data (OBJ files and orthomosaic images), are publicly available at the ETH repository: <https://www.research-collection.ethz.ch/handle/20.500.11850/686246>.

Acknowledgments

Miisa Hakkinen is acknowledged for assistance. Many thanks to Remy Lüchinger for preparing incredible thin sections. J. Hermann and S. Schmalholz are warmly acknowledged for constructive reviews and stimulating words that helped improve this paper, as well as the editor J. Dixon for efficient editorial handling. This work was supported by an ETH Career Seed Award to JMM and the financial support from ENS de Lyon to SA.

References

- Agard, P. (2021). Subduction of oceanic lithosphere in the Alps: Selective and archetypal from (slow-spreading) oceans. *Earth-Science Reviews*, 214, 103517. <https://doi.org/10.1016/j.earscirev.2021.103517>
- Andersen, T. B., Austrheim, H., Deseta, N., Silkoset, P., & Ashwal, L. D. (2014). Large subduction earthquakes along the fossil Moho in Alpine Corsica. *Geology*, 42(5), 395–398. <https://doi.org/10.1130/g35345.1>
- Angiboust, S., Agard, P., Jolivet, L., & Beyssac, O. (2009). The Zermatt-Saas ophiolite: The largest (60-km wide) and deepest (c. 70–80 km) continuous slice of oceanic lithosphere detached from a subduction zone? *Terra Nova*, 21(3), 171–180. <https://doi.org/10.1111/j.1365-3121.2009.00870.x>
- Angiboust, S., Agard, P., Yamato, P., & Raimbourg, H. (2012). Eclogite breccias in a subducted ophiolite: A record of intermediate-depth earthquakes? *Geology*, 40(8), 707–710. <https://doi.org/10.1130/g32925.1>
- Angiboust, S., & Glodny, J. (2020). Exhumation of eclogitic ophiolitic nappes in the W. Alps: New age data and implications for crustal wedge dynamics. *Lithos*, 356, 105374. <https://doi.org/10.1016/j.lithos.2020.105374>
- Angiboust, S., Kirsch, J., Oncken, O., Glodny, J., Monié, P., & Rybacki, E. (2015). Probing the transition between seismically coupled and decoupled segments along an ancient subduction interface. *Geochemistry, Geophysics, Geosystems*, 16(6), 1905–1922. <https://doi.org/10.1002/2015gc005776>
- Angiboust, S., Pettko, T., De Hoog, J. C., Caron, B., & Oncken, O. (2014). Channelized fluid flow and eclogite-facies metasomatism along the subduction shear zone. *Journal of Petrology*, 55(5), 883–916. <https://doi.org/10.1093/ptrology/egu010>
- Angiboust, S., Yamato, P., Hergarten, S., Hyppolito, T., Bebout, G. E., & Morales, L. (2017). Fluid pathways and high-*P* metasomatism in a subducted continental slice (Mt. Emilius klippe, W. Alps). *Journal of Metamorphic Geology*, 35(5), 471–492. <https://doi.org/10.1111/jmg.12241>
- Audet, P., & Bürgmann, R. (2014). Possible control of subduction zone slow-earthquake periodicity by silica enrichment. *Nature*, 510(7505), 389–392. <https://doi.org/10.1038/nature13391>
- Audet, P., & Kim, Y. (2016). Teleseismic constraints on the geological environment of deep episodic slow earthquakes in subduction zone forearcs: A review. *Tectonophysics*, 670, 1–15. <https://doi.org/10.1016/j.tecto.2016.01.005>
- Auzende, A. L., Escartin, J., Walte, N. P., Guillot, S., Hirth, G., & Frost, D. J. (2015). Deformation mechanisms of antigorite serpentinite at subduction zone conditions determined from experimentally and naturally deformed rocks. *Earth and Planetary Science Letters*, 411, 229–240. <https://doi.org/10.1016/j.epsl.2014.11.053>
- Bach, W., & Früh-Green, G. L. (2010). Alteration of the oceanic lithosphere and implications for seafloor processes. *Elements*, 6(3), 173–178. <https://doi.org/10.2113/gselements.6.3.173>
- Bedford, J. R., Moreno, M., Deng, Z., Oncken, O., Schurr, B., John, T., et al. (2020). Months-long thousand-kilometre-scale wobbling before great subduction earthquakes. *Nature*, 580(7805), 628–635. <https://doi.org/10.1038/s41586-020-2212-1>
- Behr, W. M., & Bürgmann, R. (2021). What's down there? The structures, materials and environment of deep-seated slow slip and tremor. *Philosophical Transactions of the Royal Society A*, 379(2193), 20200218. <https://doi.org/10.1098/rsta.2020.0218>
- Behr, W. M., Kotowski, A. J., & Ashley, K. T. (2018). Dehydration-induced rheological heterogeneity and the deep tremor source in warm subduction zones. *Geology*, 46(5), 475–478. <https://doi.org/10.1130/g40105.1>
- Bial, J., & Trepmann, C. A. (2013). The microstructural record of porphyroclasts and matrix of partly serpentinized peridotite mylonites—from brittle and crystal-plastic deformation to dissolution–precipitation creep. *Solid Earth*, 4(2), 315–330. <https://doi.org/10.5194/se-4-315-2013>
- Bloch, W., John, T., Kummerow, J., Salazar, P., Krüger, O. S., & Shapiro, S. A. (2018). Watching dehydration: Seismic indication for transient fluid pathways in the oceanic mantle of the subducting Nazca slab. *Geochemistry, Geophysics, Geosystems*, 19(9), 3189–3207. <https://doi.org/10.1029/2018gc007703>
- Bons, P. D., Elburg, M. A., & Gomez-Rivas, E. (2012). A review of the formation of tectonic veins and their microstructures. *Journal of Structural Geology*, 43, 33–62. <https://doi.org/10.1016/j.jsg.2012.07.005>
- Bose, K., & Navrotsky, A. (1998). Thermochemistry and phase equilibria of hydrous phases in the system MgO-SiO₂-H₂O: Implications for volatile transport to the mantle. *Journal of Geophysical Research*, 103(B5), 9713–9719. <https://doi.org/10.1029/98jb00506>
- Brantut, N., Stefanou, I., & Sulem, J. (2017). Dehydration-induced instabilities at intermediate depths in subduction zones. *Journal of Geophysical Research: Solid Earth*, 122(8), 6087–6107. <https://doi.org/10.1002/2017jb014357>
- Bucher, K., Fazis, Y., De Capitani, C., & Grapes, R. (2005). Blueschists, eclogites, and decompression assemblages of the Zermatt-Saas ophiolite: High-pressure metamorphism of subducted Tethys lithosphere. *American Mineralogist*, 90(5–6), 821–835. <https://doi.org/10.2138/am.2005.1718>
- Bucher, K., Weisenberger, T. B., Weber, S., Klemm, O., & Corfu, F. (2020). The Theodul Glacier Unit, a slab of pre-Alpine rocks in the Alpine meta-ophiolite of Zermatt-Saas, Western Alps. *Swiss Journal of Geosciences*, 113(1), 1–22. <https://doi.org/10.1186/s00015-020-00354-6>
- Cabrera, L., Ruiz, S., Poli, P., Contreras-Reyes, E., Osses, A., & Mancini, R. (2021). Northern Chile intermediate-depth earthquakes controlled by plate hydration. *Geophysical Journal International*, 226(1), 78–90. <https://doi.org/10.1093/gji/ggaa565>
- Chernak, L. J., & Hirth, G. (2011). Syndeformational antigorite dehydration produces stable fault slip. *Geology*, 39(9), 847–850. <https://doi.org/10.1130/g31919.1>
- Clarke, E., De Hoog, J. C. M., Kirstein, L. A., Harvey, J., & Debret, B. (2020). Metamorphic olivine records external fluid infiltration during serpentinite dehydration. *Geochemical Perspectives Letters*, 16, 25–29. <https://doi.org/10.7185/geochemlet.2039>
- Clément, M., Padrón-Navarta, J. A., & Tommasi, A. (2019). Interplay between fluid extraction mechanisms and antigorite dehydration reactions (Val Malenco, Italian Alps). *Journal of Petrology*, 60(10), 1935–1962. <https://doi.org/10.1093/ptrology/egz058>
- Craiu, A., Ferrand, T. P., Manea, E. F., Vrijmoed, J. C., & Märmureanu, A. (2022). A switch from horizontal compression to vertical extension in the Vrancea slab explained by the volume reduction of serpentine dehydration. *Scientific Reports*, 12(1), 22320. <https://doi.org/10.1038/s41598-022-26260-5>
- Dal Piaz, G. V., & Ernst, W. G. (1978). Areal geology and petrology of eclogites and associated metabasites of the Piemonte ophiolite nappe, breuil–St. Jacques area, Italian Western Alps. *Tectonophysics*, 51(1–2), 99–126. [https://doi.org/10.1016/0040-1951\(78\)90053-7](https://doi.org/10.1016/0040-1951(78)90053-7)
- Davies, J. H. (1999). The role of hydraulic fractures and intermediate-depth earthquakes in generating subduction-zone magmatism. *Nature*, 398(6723), 142–145. <https://doi.org/10.1038/18202>
- Delbridge, B. G., Houston, H., Bürgmann, R., Kita, S., & Asano, Y. (2024). A weak subducting slab at intermediate depths below northeast Japan. *Science Advances*, 10(9), eadh2106. <https://doi.org/10.1126/sciadv.adh2106>
- de Meyer, C. M., Baumgartner, L. P., Beard, B. L., & Johnson, C. M. (2014). Rb–Sr ages from phengite inclusions in garnets from high pressure rocks of the Swiss Western Alps. *Earth and Planetary Science Letters*, 395, 205–216. <https://doi.org/10.1016/j.epsl.2014.03.050>

- Dobson, D. P., Meredith, P. G., & Boon, S. A. (2002). Simulation of subduction zone seismicity by dehydration of serpentine. *Science*, 298(5597), 1407–1410. <https://doi.org/10.1126/science.1075390>
- Dragovic, B., Angiboust, S., & Tappa, M. J. (2020). Petrochronological close-up on the thermal structure of a paleo-subduction zone (W. Alps). *Earth and Planetary Science Letters*, 547, 116446. <https://doi.org/10.1016/j.epsl.2020.116446>
- Eberhard, L., Plümper, O., & Frost, D. J. (2023). Early release of H₂O during subduction of carbonated ultramafic lithologies. *Contributions to Mineralogy and Petrology*, 178(3), 17. <https://doi.org/10.1007/s00410-023-01997-y>
- Ferrand, T. P., Hilairet, N., Incel, S., Deldicque, D., Labrousse, L., Gasc, J., et al. (2017). Dehydration-driven stress transfer triggers intermediate-depth earthquakes. *Nature Communications*, 8(1), 15247. <https://doi.org/10.1038/ncomms15247>
- Fontana, E., Panseri, M., & Tartarotti, P. (2008). Oceanic relict textures in the Mount Avic serpentinites, Western Alps. *Ophioliti*, 33(2), 105–118.
- French, M. E., Hirth, G., & Okazaki, K. (2019). Fracture-induced pore fluid pressure weakening and dehydration of serpentinite. *Tectonophysics*, 767, 228168. <https://doi.org/10.1016/j.tecto.2019.228168>
- Früh-Green, G. L., Connolly, J. A., Plas, A., Kelley, D. S., & Grobety, B. (2004). Serpentinization of oceanic peridotites: Implications for geochemical cycles and biological activity. *The Subseafloor Biosphere at Mid-Ocean Ridges*, 144, 119–136. <https://doi.org/10.1029/144gm08>
- Gasc, J., Hilairet, N., Yu, T., Ferrand, T., Schubnel, A., & Wang, Y. (2017). Faulting of natural serpentinite: Implications for intermediate-depth seismicity. *Earth and Planetary Science Letters*, 474, 138–147. <https://doi.org/10.1016/j.epsl.2017.06.016>
- Gilio, M., Scambelluri, M., Agostini, S., Godard, M., Peters, D., & Pettke, T. (2019). Petrology and geochemistry of serpentinites associated with the ultra-high pressure Lago di Cignana Unit (Italian Western Alps). *Journal of Petrology*, 60(6), 1229–1262. <https://doi.org/10.1093/ptrology/egz030>
- Grevemeyer, I., Ranero, C. R., & Ivandic, M. (2018). Structure of oceanic crust and serpentinization at subduction trenches. *Geosphere*, 14(2), 395–418. <https://doi.org/10.1130/ges01537.1>
- Groppo, C., Beltrando, M., & Compagnoni, R. (2009). The P–T path of the ultra-high pressure Lago Di Cignana and adjoining high-pressure meta-ophiolitic units: Insights into the evolution of the subducting Tethyan slab. *Journal of Metamorphic Geology*, 27(3), 207–231. <https://doi.org/10.1111/j.1525-1314.2009.00814.x>
- Gutiérrez-Aguilar, F., Hernández-Urbe, D., Holder, R. M., & Condit, C. B. (2022). Fluid-induced fault reactivation due to Brucite+ antigorite dehydration triggered the Mw7.1 September 19th Puebla-Morelos (Mexico) intermediate-depth earthquake. *Geophysical Research Letters*, 49(20), e2022GL100814. <https://doi.org/10.1029/2022gl100814>
- Hacker, B. R., Peacock, S. M., Abers, G. A., & Holloway, S. D. (2003). Subduction factory 2. Are intermediate-depth earthquakes in subducting slabs linked to metamorphic dehydration reactions? *Journal of Geophysical Research*, 108(B1), 2030. <https://doi.org/10.1029/2001jb001129>
- Hasegawa, A., & Nakajima, J. (2017). Seismic imaging of slab metamorphism and genesis of intermediate-depth intraslab earthquakes. *Progress in Earth and Planetary Science*, 4(1), 12. <https://doi.org/10.1186/s40645-017-0126-9>
- Healy, D., Reddy, S. M., Timms, N. E., Gray, E. M., & Brovarone, A. V. (2009). Trench-parallel fast axes of seismic anisotropy due to fluid-filled cracks in subducting slabs. *Earth and Planetary Science Letters*, 283(1–4), 75–86. <https://doi.org/10.1016/j.epsl.2009.03.037>
- Hermann, J., Müntener, O., & Scambelluri, M. (2000). The importance of serpentine mylonites for subduction and exhumation of oceanic crust. *Tectonophysics*, 327(3–4), 225–238. [https://doi.org/10.1016/s0040-1951\(00\)00171-2](https://doi.org/10.1016/s0040-1951(00)00171-2)
- Hirauchi, K. I., Katayama, I., & Kouketsu, Y. (2020). Semi-brittle deformation of antigorite serpentinite under forearc mantle wedge conditions. *Journal of Structural Geology*, 140, 104151. <https://doi.org/10.1016/j.jsg.2020.104151>
- Huber, K., Vrijmoed, J. C., & John, T. (2022). Formation of olivine veins by reactive fluid flow in a dehydrating serpentinite. *Geochemistry, Geophysics, Geosystems*, 23(6), e2021GC010267. <https://doi.org/10.1029/2021gc010267>
- Isacks, B., & Molnar, P. (1971). Distribution of stresses in the descending lithosphere from a global survey of focal-mechanism solutions of mantle earthquakes. *Reviews of Geophysics*, 9(1), 103–174. <https://doi.org/10.1029/rg009i001p0103>
- Isacks, B. L., & Barazangi, M. (1977). Geometry of Benioff zones: Lateral segmentation and downwards bending of the subducted lithosphere. *Island Arcs, Deep Sea Trenches and Back-Arc Basins*, 1, 99–114. <https://doi.org/10.1029/me001p0099>
- Jabaloy-Sánchez, A., Sánchez-Vizcaíno, V. L., Padrón-Navarta, J. A., Hidas, K., Gómez-Pugnaire, M. T., & Garrido, C. J. (2022). Olivine-rich veins in high-pressure serpentinites: A far-field paleo-stress snapshot during subduction. *Journal of Structural Geology*, 163, 104721. <https://doi.org/10.1016/j.jsg.2022.104721>
- John, T., & Schenk, V. (2006). Interrelations between intermediate-depth earthquakes and fluid flow within subducting oceanic plates: Constraints from eclogite facies pseudotachylytes. *Geology*, 34(7), 557–560. <https://doi.org/10.1130/g22411a.1>
- Jung, H., & Green, H. W. (2004). Experimental faulting of serpentinite during dehydration: Implications for earthquakes, seismic low-velocity zones, and anomalous hypocenter distributions in subduction zones. *International Geology Review*, 46(12), 1089–1102. <https://doi.org/10.2747/0020-6814.46.12.1089>
- Jung, H., Green, H. W., & Dobrzhinetskaya, L. F. (2004). Intermediate-depth earthquake faulting by dehydration embrittlement with negative volume change. *Nature*, 428(6982), 545–549. <https://doi.org/10.1038/nature02412>
- Kawano, S., Katayama, I., & Okazaki, K. (2011). Permeability anisotropy of serpentinite and fluid pathways in a subduction zone. *Geology*, 39(10), 939–942. <https://doi.org/10.1130/g32173.1>
- Kempf, E. D., Hermann, J., Reusser, E., Baumgartner, L. P., & Lanari, P. (2020). The role of the antigorite+ brucite to olivine reaction in subducted serpentinites (Zermatt, Switzerland). *Swiss Journal of Geosciences*, 113(1), 1–36. <https://doi.org/10.1186/s00015-020-00368-0>
- Klein, F., Humphris, S. E., & Bach, W. (2020). Brucite formation and dissolution in oceanic serpentinite. *Geochemical Perspectives Letters*, 16, 1–5. <https://doi.org/10.7185/geochemlet.2035>
- Lagabrielle, Y., & Cannat, M. (1990). Alpine Jurassic ophiolites resemble the modern central Atlantic basement. *Geology*, 18(4), 319–322. [https://doi.org/10.1130/0091-7613\(1990\)018<0319:ajortm>2.3.co;2](https://doi.org/10.1130/0091-7613(1990)018<0319:ajortm>2.3.co;2)
- Li, X. P., Rahn, M., & Bucher, K. (2004). Serpentinites of the Zermatt-Saas ophiolite complex and their texture evolution. *Journal of Metamorphic Geology*, 22(3), 159–177. <https://doi.org/10.1111/j.1525-1314.2004.00503.x>
- López Sánchez-Vizcaíno, V., Trommsdorff, V., Gómez-Pugnaire, M. T., Garrido, C. J., Müntener, O., & Connolly, J. A. D. (2005). Petrology of titanian clinohumite and olivine at the high-pressure breakdown of antigorite serpentinite to chlorite harzburgite (Almirez Massif, S. Spain). *Contributions to Mineralogy and Petrology*, 149(6), 627–646. <https://doi.org/10.1007/s00410-005-0678-3>
- Luoni, P., Rebay, G., Spalla, M. I., & Zanoni, D. (2018). UHP Ti-chondroite in the Zermatt-Saas serpentinite: Constraints on a new tectonic scenario. *American Mineralogist: Journal of Earth and Planetary Materials*, 103(6), 1002–1005. <https://doi.org/10.2138/am-2018-6460>
- Luoni, P., Zanoni, D., Rebay, G., & Spalla, M. I. (2019). Deformation history of ultra high-pressure ophiolitic serpentinites in the Zermatt-Saas Zone, Créton, Upper Valtournanche (Aosta Valley, Western Alps). *Ophioliti*, 44(2), 111–123.
- Malvoisin, B. (2015). Mass transfer in the oceanic lithosphere: Serpentinization is not isochemical. *Earth and Planetary Science Letters*, 430, 75–85. <https://doi.org/10.1016/j.epsl.2015.07.043>

- McGary, R. S., Evans, R. L., Wannamaker, P. E., Elsenbeck, J., & Rondenay, S. (2014). Pathway from subducting slab to surface for melt and fluids beneath Mount Rainier. *Nature*, *511*(7509), 338–340. <https://doi.org/10.1038/nature13493>
- Menant, A., Angiboust, S., & Gerya, T. (2019). Stress-driven fluid flow controls long-term megathrust strength and deep accretionary dynamics. *Scientific Reports*, *9*(1), 9714. <https://doi.org/10.1038/s41598-019-46191-y>
- Moreno, M., Haberland, C., Oncken, O., Rietbrock, A., Angiboust, S., & Heidbach, O. (2014). Locking of the Chile subduction zone controlled by fluid pressure before the 2010 earthquake. *Nature Geoscience*, *7*(4), 292–296. <https://doi.org/10.1038/ngeo2102>
- Muñoz-Montecinos, J., Angiboust, S., Cambeses, A., & García-Casco, A. (2020). Multiple veining in a paleo-accretionary wedge: The metamorphic rock record of prograde dehydration and transient high pore-fluid pressures along the subduction interface (Western Series, central Chile). *Geosphere*, *16*(3), 765–786. <https://doi.org/10.1130/ges02227.1>
- Muñoz-Montecinos, J., Angiboust, S., & García-Casco, A. (2021). Blueschist-facies paleo-earthquakes in a serpentinite channel (Zagros suture, Iran) enlighten seismogenesis in Mariana-type subduction margins. *Earth and Planetary Science Letters*, *573*, 117135. <https://doi.org/10.1016/j.epsl.2021.117135>
- Muñoz-Montecinos, J., Angiboust, S., García-Casco, A., Glodny, J., & Bebout, G. (2021). Episodic hydrofracturing and large-scale flushing along deep subduction interfaces: Implications for fluid transfer and carbon recycling (Zagros Orogen, southeastern Iran). *Chemical Geology*, *571*, 120173. <https://doi.org/10.1016/j.chemgeo.2021.120173>
- Muñoz-Montecinos, J., Angiboust, S., García-Casco, A., & Raimondo, T. (2023). Shattered veins elucidate brittle creep processes in the deep slow slip and tremor region. *Tectonics*, *42*(4), e2022TC007605. <https://doi.org/10.1029/2022tc007605>
- Muñoz-Montecinos, J., & Behr, W. M. (2023). Transient permeability of a deep-seated subduction interface shear zone. *Geophysical Research Letters*, *50*(20), e2023GL104244. <https://doi.org/10.1029/2023gl104244>
- Nagaya, T., Okamoto, A., Kido, M., Muto, J., & Wallis, S. R. (2022). Dehydration of brucite+ antigorite under mantle wedge conditions: Insights from the direct comparison of microstructures before and after experiments. *Contributions to Mineralogy and Petrology*, *177*(9), 87. <https://doi.org/10.1007/s00410-022-01956-z>
- Negro, F., Bousquet, R., Vils, F., Pellet, C. M., & Hänggi-Schaub, J. (2013). Thermal structure and metamorphic evolution of the Piemont-Ligurian metasediments in the northern Western Alps. *Swiss Journal of Geosciences*, *106*(1), 63–78. <https://doi.org/10.1007/s00015-013-0119-7>
- Okazaki, K., & Hirth, G. (2016). Dehydration of lawsonite could directly trigger earthquakes in subducting oceanic crust. *Nature*, *530*(7588), 81–84. <https://doi.org/10.1038/nature16501>
- Oncken, O., Angiboust, S., & Dresen, G. (2022). Slow slip in subduction zones: Reconciling deformation fabrics with instrumental observations and laboratory results. *Geosphere*, *18*(1), 104–129. <https://doi.org/10.1130/ges02382.1>
- Padrón-Navarta, J. A., Lopez Sanchez-Vizcaíno, V., Garrido, C. J., & Gómez-Pugnaire, M. T. (2011). Metamorphic record of high-pressure dehydration of antigorite serpentinite to chlorite harzburgite in a subduction setting (Cerro del Almirez, Nevado-Filábride Complex, Southern Spain). *Journal of Petrology*, *52*(10), 2047–2078. <https://doi.org/10.1093/petrology/egr039>
- Padrón-Navarta, J. A., Sánchez-Vizcaíno, V. L., Hermann, J., Connolly, J. A., Garrido, C. J., Gómez-Pugnaire, M. T., & Marchesi, C. (2013). Tschermak's substitution in antigorite and consequences for phase relations and water liberation in high-grade serpentinites. *Lithos*, *178*, 186–196. <https://doi.org/10.1016/j.lithos.2013.02.001>
- Peacock, S. M., & Hyndman, R. D. (1999). Hydrous minerals in the mantle wedge and the maximum depth of subduction thrust earthquakes. *Geophysical Research Letters*, *26*(16), 2517–2520. <https://doi.org/10.1029/1999gl900558>
- Perrillat, J. P., Daniel, I., Koga, K. T., Reynard, B., Cardon, H., & Crichton, W. A. (2005). Kinetics of antigorite dehydration: A real-time X-ray diffraction study. *Earth and Planetary Science Letters*, *236*(3–4), 899–913. <https://doi.org/10.1016/j.epsl.2005.06.006>
- Peters, D., Bretscher, A., John, T., Scambelluri, M., & Pettker, T. (2017). Fluid-mobile elements in serpentinites: Constraints on serpentinisation environments and element cycling in subduction zones. *Chemical Geology*, *466*, 654–666. <https://doi.org/10.1016/j.chemgeo.2017.07.017>
- Peters, D., Pettker, T., John, T., & Scambelluri, M. (2020). The role of brucite in water and element cycling during serpentinite subduction—Insights from Erro Tobbio (Liguria, Italy). *Lithos*, *360*, 105431. <https://doi.org/10.1016/j.lithos.2020.105431>
- Plümper, O., John, T., Podladchikov, Y. Y., Vrijmoed, J. C., & Scambelluri, M. (2017). Fluid escape from subduction zones controlled by channel-forming reactive porosity. *Nature Geoscience*, *10*(2), 150–156. <https://doi.org/10.1038/ngeo2865>
- Plümper, O., Røyne, A., Magrasó, A., & Jamtveit, B. (2012). The interface-scale mechanism of reaction-induced fracturing during serpentinization. *Geology*, *40*(12), 1103–1106. <https://doi.org/10.1130/g33390.1>
- Proctor, B., & Hirth, G. (2016). “Ductile to brittle” transition in thermally stable antigorite gouge at mantle pressures. *Journal of Geophysical Research: Solid Earth*, *121*(3), 1652–1663. <https://doi.org/10.1002/2015jb012710>
- Reddy, S., Wheeler, J., & Cliff, R. (1999). The geometry and timing of orogenic extension: An example from the Western Italian Alps. *Journal of Metamorphic Geology*, *17*(5), 573–590. <https://doi.org/10.1046/j.1525-1314.1999.00220.x>
- Reynard, B. (2013). Serpentine in active subduction zones. *Lithos*, *178*, 171–185. <https://doi.org/10.1016/j.lithos.2012.10.012>
- Rubatto, D., Gebauer, D., & Fanning, M. (1998). Jurassic formation and Eocene subduction of the Zermatt–Saas–Fee ophiolites: Implications for the geodynamic evolution of the Central and Western Alps. *Contributions to Mineralogy and Petrology*, *132*(3), 269–287. <https://doi.org/10.1007/s004100050421>
- Scambelluri, M., Pettker, T., Rampone, E., Godard, M., & Reusser, E. (2014). Petrology and trace element budgets of high-pressure peridotites indicate subduction dehydration of serpentinized mantle (Cima di Gagnone, Central Alps, Switzerland). *Journal of Petrology*, *55*(3), 459–498. <https://doi.org/10.1093/petrology/egt068>
- Schmalholz, S. M., Moulas, E., Räss, L., & Müntener, O. (2023). Serpentinite dehydration and olivine vein formation during ductile shearing: Insights from 2D numerical modeling on porosity generation, density variations, and transient weakening. *Journal of Geophysical Research: Solid Earth*, *128*(11), e2023JB026985. <https://doi.org/10.1029/2023jb026985>
- Schmidt, M., & Poli, S. (2013). Devolatilization during subduction. In *Treatise on geochemistry, The crust* (Vol. 4, pp. 669–701). Elsevier. <https://doi.org/10.1016/b978-0-08-095975-7.00321-1>
- Schmidt, M. W., & Poli, S. (1998). Experimentally based water budgets for dehydrating slabs and consequences for arc magma generation. *Earth and Planetary Science Letters*, *163*(1–4), 361–379. [https://doi.org/10.1016/s0012-821x\(98\)00142-3](https://doi.org/10.1016/s0012-821x(98)00142-3)
- Schwartz, S., Guillot, S., Reynard, B., Lafay, R., Debret, B., Nicolle, C., et al. (2013). Pressure–temperature estimates of the lizardite/antigorite transition in high pressure serpentinites. *Lithos*, *178*, 197–210. <https://doi.org/10.1016/j.lithos.2012.11.023>
- Shelly, D. R., Beroza, G. C., Ide, S., & Nakamura, S. (2006). Low-frequency earthquakes in Shikoku, Japan, and their relationship to episodic tremor and slip. *Nature*, *442*(7099), 188–191. <https://doi.org/10.1038/nature04931>
- Shen, T., Hermann, J., Zhang, L., Lü, Z., Padrón-Navarta, J. A., Xia, B., & Bader, T. (2015). UHP metamorphism documented in Ti-chondroditic and Ti-clinohumite-bearing serpentinized ultramafic rocks from Chinese southwestern Tianshan. *Journal of Petrology*, *56*(7), 1425–1458. <https://doi.org/10.1093/petrology/egv042>

- Sibson, R. H. (2013). Stress switching in subduction forearcs: Implications for overpressure containment and strength cycling on megathrusts. *Tectonophysics*, *600*, 142–152. <https://doi.org/10.1016/j.tecto.2013.02.035>
- Sippl, C., Dielforder, A., John, T., & Schmalholz, S. M. (2022). Global constraints on intermediate-depth intraslab stresses from slab geometries and mechanisms of double seismic zone earthquakes. *Geochemistry, Geophysics, Geosystems*, *23*(9), e2022GC010498. <https://doi.org/10.1029/2022gc010498>
- Skora, S., Mahlen, N. J., Johnson, C. M., Baumgartner, L. P., Lapen, T. J., Beard, B. L., & Szilvagy, E. T. (2015). Evidence for protracted prograde metamorphism followed by rapid exhumation of the Zermatt-Saas Fee ophiolite. *Journal of Metamorphic Geology*, *33*(7), 711–734. <https://doi.org/10.1111/jmg.12148>
- Steck, A., Masson, H., & Robyr, M. (2015). Tectonics of the Monte Rosa and surrounding nappes (Switzerland and Italy): Tertiary phases of subduction, thrusting and folding in the Pennine Alps. *Swiss Journal of Geosciences*, *108*(1), 3–34. <https://doi.org/10.1007/s00015-015-0188-x>
- Taetz, S., John, T., Bröcker, M., Spandler, C., & Stracke, A. (2018). Fast intraslab fluid-flow events linked to pulses of high pore fluid pressure at the subducted plate interface. *Earth and Planetary Science Letters*, *482*, 33–43. <https://doi.org/10.1016/j.epsl.2017.10.044>
- Tarling, M. S., Smith, S. A., & Scott, J. M. (2019). Fluid overpressure from chemical reactions in serpentinite within the source region of deep episodic tremor. *Nature Geoscience*, *12*(12), 1034–1042. <https://doi.org/10.1038/s41561-019-0470-z>
- Trommsdorff, V., & Evans, B. W. (1980). Titanian hydroxyl-clinohumite: Formation and breakdown in antigorite rocks (Malenco, Italy). *Contributions to Mineralogy and Petrology*, *72*(3), 229–242. <https://doi.org/10.1007/bf00376142>
- Ulmer, P., & Trommsdorff, V. (1995). Serpentine stability to mantle depths and subduction-related magmatism. *Science*, *268*(5212), 858–861. <https://doi.org/10.1126/science.268.5212.858>
- Ulrich, M., Rubatto, D., Hermann, J., Markmann, T. A., Bouvier, A. S., & Deloule, E. (2024). Olivine formation processes and fluid pathways in subducted serpentinites revealed by in-situ oxygen isotope analysis (Zermatt-Saas, Switzerland). *Chemical Geology*, *649*, 121978. <https://doi.org/10.1016/j.chemgeo.2024.121978>
- Wagner, L. S., Caddick, M. J., Kumar, A., Beck, S. L., & Long, M. D. (2020). Effects of oceanic crustal thickness on intermediate depth seismicity. *Frontiers in Earth Science*, *8*, 244. <https://doi.org/10.3389/feart.2020.00244>
- Wang, K., Huang, T., Tilmann, F., Peacock, S. M., & Lange, D. (2020). Role of Serpentinized mantle wedge in affecting Megathrust Seismogenic behavior in the area of the 2010 $M=8.8$ Maule earthquake. *Geophysical Research Letters*, *47*(22), e2020GL090482. <https://doi.org/10.1029/2020gl090482>
- Wassmann, S., Stöckert, B., & Trepmann, C. A. (2011). Dissolution precipitation creep versus crystalline plasticity in high-pressure metamorphic serpentinites. *Geological Society, London, Special Publications*, *360*(1), 129–149. <https://doi.org/10.1144/sp360.8>
- Whitney, D. L., & Evans, B. W. (2010). Abbreviations for names of rock-forming minerals. *American Mineralogist*, *95*(1), 185–187. <https://doi.org/10.2138/am.2010.3371>
- Woodcock, N. H., & Mort, K. (2008). Classification of fault breccias and related fault rocks. *Geological Magazine*, *145*(3), 435–440. <https://doi.org/10.1017/s0016756808004883>